Article

Seismic Sequence Analysis of the Arraiolos Zone, South Portugal, and Its Seismotectonic Implications: A Detailed Analysis of the Period 15 January–30 June 2018

Piedade Wachilala [1,2,*] , **José Borges** [2,3,4] , **Bento Caldeira** [2,3,4] **and Mourad Bezzeghoud** [2,3,4]

1 Higher Institute of Education Science of the Huíla—ISCED-Huíla, Department of Teaching and Investigation of Exact and Natural Sciences, Sarmento Rodrigues Street, Nº. 2, Lubango P.O. Box 230, Angola

2 Instituto de Ciências da Terra (ICT), Universidade de Évora, Apartado 94, 7002-554 Évora, Portugal; jborges@uevora.pt (J.B.); bafcc@uevora.pt (B.C.); mourad@uevora.pt (M.B.)

3 Departamento de Física, Escola de Ciências e Tecnologia, Universidade de Évora, Apartado 94, 7002-554 Évora, Portugal

4 Earth and Remote Sensing Laboratory (EARSLab), University of Évora, 7004-516 Évora, Portugal

* Correspondence: piedade.wachilala@isced-huila.ed.ao

Abstract: The Arraiolos Zone has been affected by the persistent superficial seismicity (focal depth < 20 km) of a weak magnitude (M < 4) and some events of a higher magnitude (M > 4), and is mainly located around the Aldeia da Serra village. On 15 January 2018, at 11:51 UTC, the largest instrumental earthquake recorded in that area occurred, with a magnitude (ML 4.9) located northeast of Arraiolos, near the Aldeia da Serra village. This event was followed by a sequence of aftershocks with a magnitude (ML) ≤ 3.5. This seismic sequence was monitored by the designated temporary seismic network of Arraiolos, comprising 12 broadband seismic stations (CMG 6TD, 30 s) from the ICT (Institute of Earth Sciences, Évora) and 21 short-period stations (CDJ 2.0 Hz) from the IDL (Instituto Dom Luiz), distributed around the epicenter, within a radius of approximately 25 km. To infer the structure and kinematics of faults at depth and to constrain the crustal stress field in which the earthquakes occur, we use the polarities of the first P-wave arrivals and the S/P amplitude ratios to better constrain the focal mechanisms of 54 events selected, and apply the HASH algorithm. Overall, the good-quality (defined by the HASH parameters) focal solutions are characterized by a mixture of reverse and strike-slip mechanisms in our study area (AZS). Our seismicity and focal mechanism results suggest that the horizontal stress is more dominant than the vertical one and oriented in the NW–SE direction, parallel with the strike of the main faults. This analysis leads us to affirm that the ASZ is an active right-lateral shear zone.

Keywords: seismicity; focal mechanisms; seismotectonic implications; Arraiolos seismic zone

1. Introduction

The seismicity data and the focal mechanisms are considered fundamental seismic parameters for the characterization of the geodynamics of the region surrounding the seismic source [1,2]. The understanding of tectonic fault systems and the study of seismic sequences can be useful for seismic hazard studies and stress regime change [3–7].

The Arraiolos zone, located in Central Alentejo (Southern Portugal), presents a persistent superficial seismicity (depth < 20 km) of a low magnitude (M < 4) and some events of a higher magnitude (M > 4), and is found essentially concentrated in the Aldeia da Serra area. This seismicity, despite being of low magnitude, is significant in the regional context. In an attempt to understand this seismic behavior that contrasts with the regional pattern, this area has been the object of several studies in the fields of seismicity, geology, and tectonics, among which, [1,2,8–12] for the characterization of its complex geodynamics. More recently, Hamak et al. [13] started to carry out the first seismic tomography

studies in the Arraiolos zone, with the purpose of detecting geological faults that may be responsible for the region's seismicity. However, given the nature of the seismicity and the deficient azimuthal coverage of the seismic network, in recent years, the correlation between the seismicity of the region and any of the existing geological features has been a major challenge. This complexity in understanding tectonic events creates some difficulty in seismological interpretation. In this context, it is necessary to seek a tectonic explanation for its origin, namely, to understand its relationship with existing geological faults, which may correspond to active faults, or simple lineaments. Several studies carried out in tectonically active mountainous areas, for example [14], suggest that in addition to the surficial deformations and risks that earthquakes can cause, they also influence the hydrogeological conditions of a region.

As mentioned by several authors, e.g., [15], detailed studies on the spatiotemporal evolutions of aftershocks provide important information on the main characteristics of main shock ruptures [16,17]. Furthermore, aftershocks are usually triggered by direct stress transfer from the main shock or by post-seismic deformation induced by the main shock [18]. Therefore, a detailed knowledge of the spatiotemporal evolution of aftershock sequences helps to better understand the fundamental physics of the interaction between earthquakes and the prediction and mitigation of seismic risks [19]. On the other hand, it is important to determine the focal mechanisms of small earthquakes as accurately as possible. There are different methods for its determination, using the polarity of the P-wave, with or without shear wave polarization (S), S/P wave amplitude ratios and moment tensor determination by full waveform inversion (moment tensor inversion) [20]. The application of these methods depends on the availability of data and the purpose of the study. In addition to the polarities of the first P wave motion [21,22], several studies have also used S/P amplitude relationships to determine the focal mechanisms, e.g., [23], which concluded that the inclusion of amplitude data improves the solutions for the focal mechanisms of small earthquakes.

In this study, a detailed analysis was carried out on the seismic sequence of the magnitude (ML 4.9) of the earthquake of Arraiolos of 15 January 2018 in the northeast region of Arraiolos, near the village of Aldeia da Serra. The hypocentral source parameters of the main shock (Table 1) were previously determined by the Instituto Português do Mar e da Atmosfera (IPMA).

Table 1. Hypocentral source parameters of main shock determined by IPMA.

Date (yy/mm/dd)	Hour (hh:mm)	Long. (°W)	Lat. (°N)	Depth (km)	Res. (s)	Mag. (ML)	Strike	Dip	Rake
2018/01/15	11:51:40.20	−7.932	38.792	11.0	0.43	4.9	96.0	85.0	−178.0

To the data from the national seismic network (IPMA), we joined data from two seismic stations closest to the epicenter, to relocate the main shock, resulting in the following coordinates: 38.783N and 7.949W at ~12 km depth, and Rms 0.30 s, with an epicentral difference of approximately 2 km (see forward in Section 4.1).

This earthquake was widely felt in the Center and South of mainland Portugal, without causing material or human damage. In Aldeia da Serra (the epicenter zone), it was felt with a maximum intensity (MMI) of VI, which represents a vibration level classified as quite strong, and felt with an intensity of IV/V in the city of Évora, located about 20 km from the epicenter. This event was also felt with intensity III in some cities away from the epicenter, as is the case of Lisbon, located to the west, more than 100 km from the epicenter. In the localities closest to the epicenter, the event caused panic among the population, that had not felt an earthquake with a strong vibration in recent years.

This event triggered a sequence of aftershocks with a magnitude (ML) ≤ 3.5, recorded by the Arraiolos temporary seismic network. This temporary network, deployed a few days after the occurrence of the main shock, consists of 33 stations, 12 broadband stations (CMG

6TD, 30 s, belonging to UE), and 21 short-period stations (CDJ 2.0 Hz, belonging to the IDL) (see description in Section 3), distributed in a radius of approximately 30 km around the epicenter, with a view to improving the azimuthal coverage of low magnitude events and decreasing the network's detectability threshold. This temporary seismic network provided us with high-quality seismological data, which allowed us to characterize the spatiotemporal evolution of this seismic sequence and the respective focal mechanisms, determined through the polarities of the first movement of the P wave and S/P amplitude ratios, based on the method by Hardebeck and Shear [21,23]. Additionally, an explanatory model for seismicity and its articulation with tectonics and local geodynamics was suggested through the incorporation of the obtained results. This study has as main objective to characterize the seismotectonics and geodynamics of this region, whose seismicity is significant in the Portuguese mainland panorama.

2. Geological and Seismotectonic Framework

The study region falls within the tectonic domain of the Ossa-Morena Zone (MOZ). The geological composition of this tectonic domain is mainly associated with the Variscan Orogeny of late Paleozoic age (480–290 Ma) [24]. This orogenic cycle was the result of the collision of the supercontinent Gondwana with Laurasia, and the closing of the Rheic Ocean [25,26], and was responsible for defining the structure of the Iberian Massif [27], in which rocks of Precambrian and Paleozoic age outcrop. The evolution of OMZ is essentially characterized by the development of sedimentary basins, during the Carboniferous, after the collision between Gondwana and Laurasia. OMZ was formed in an extensional regime and was accompanied by deep crustal metamorphism [28] and witnessed by typical continental "rifting" magmatism [24]. The various geophysical studies carried out, e.g., [29–32], suggest that carboniferous magmatism is responsible for the placement of large amounts of magma at mid-crustal depths (12–14 km) in the region [10].

The current seismicity in mainland Portugal and, in particular, in the study zone (Figure 1) seems to be related to the slow onshore intraplate deformation (~1 mm/year or less) driven by the offshore oblique convergence of the Eurasian and Nubian plates which occurs at a rate of about 5 mm/year [1,33–37]. Figure 1 shows the instrumental seismicity of the study region (intraplate zone) in the context of Mainland Portugal and the identification of the Arraiolos Seismic Zone (ASZ) and Évora Seismic Zone (ESZ), with the record of seismicity of all magnitudes for the period of 1961–2018 and the first focal mechanisms determined in the study region [1,38]. For the focal mechanism data obtained from the 1997 and 1998 events (Figure 1b), they are of the strike-slip type with planes oriented in the NS and EW directions, which are compatible with the first tectonic model for the Arraiolos region, proposed by [8]. The seismicity of the region known as the Arraiolos seismic zone (ASZ) occurs in a region cut by numerous faults between different lithologies, located in the Évora Massif, near the border of the Lower Tagus Basin (Figures 1 and 2) [9].

In this region, some important geological structures stand out, with geomorphological evidence of activity, namely: the Lineament of São Gregório (facing north), the escarpment of Aldeia da Serra (facing west), and the Ciborro Fault (see Figure 2). In particular, this last morphotectonic structure, whose escarpment is oriented in the NW–SE direction, facing NE, with elevations in the order of 50–60 m [8], in the extreme west and to the north, places the limit of the Lower Tagus Basin locally, constituted by sedimentary rocks, with the Paleozoic base (Figure 2) which corresponds mainly to Hercynian granites [39], which are generally of the medium-to-coarse-grained porphyroid. The remaining outcropping formations are more recent, and with good cartographic expression [9]. The Évora Massif (a sub-unit of the Ossa-Morena Zone) outcrops in the Ciborro region, and consists essentially of metamorphic and igneous rocks, and is also composed of a wide variety of plutonic massifs implanted where there is a lower level of carbon dioxide. Tonalites and granodiorites predominate, which are often accompanied by granites, but the presence of gabbro-diorite bodies is also recorded [28,40].
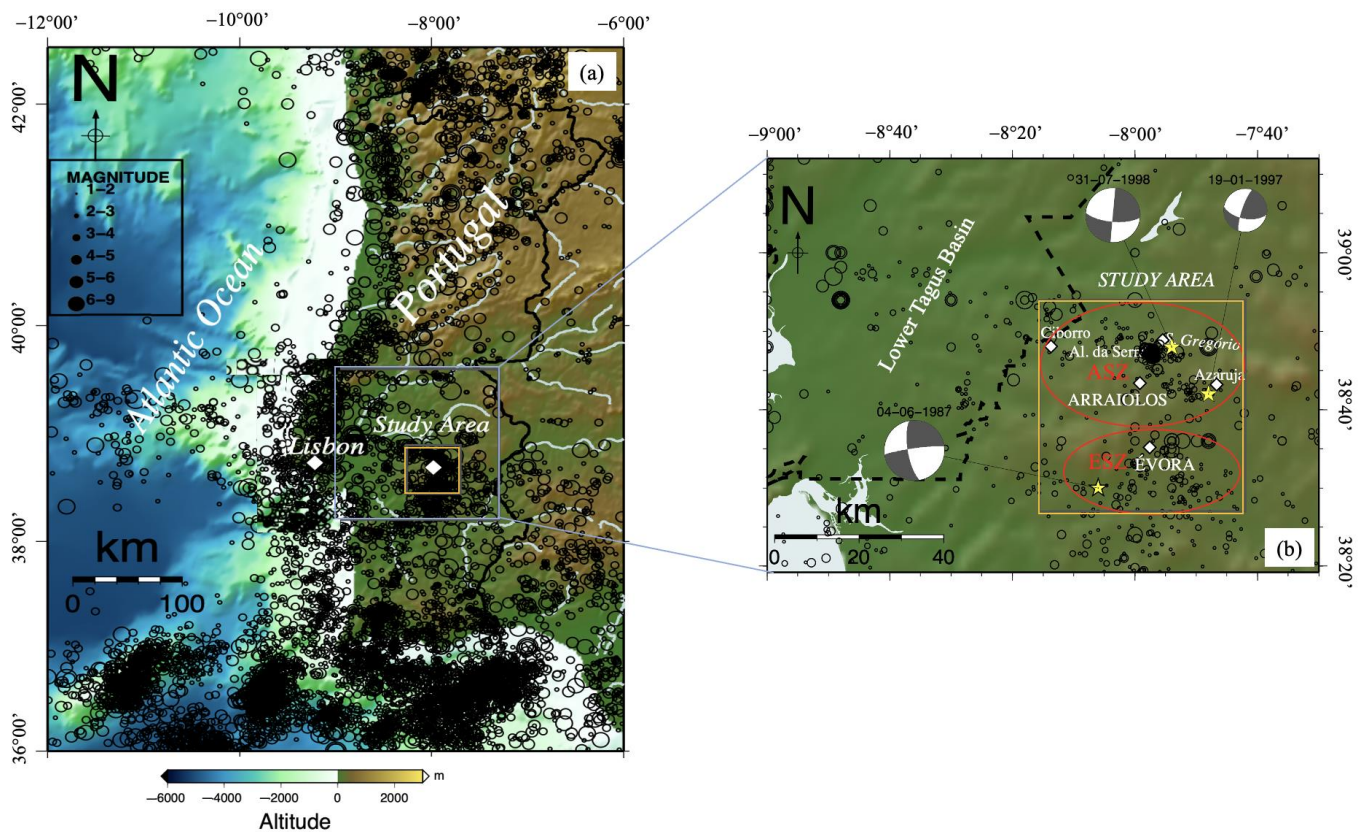
Figure 1. Regional setting of the study area. (**a**) Recorded seismicity for the period 1961–2018 in mainland Portugal and Atlantic margin, from IPMA's catalogue. (**b**) Location of the study area and the identification of seismic zones (red circles), namely: Arraiolos Seismic Zone (ASZ) and Évora Seismic Zone (ESZ), and first focal mechanisms in the study zone of events 19–01–1997 (ML = 3.2); 31–07–1998 (ML = 4.0) in ASZ, determined by [1] and 04–06–1987 (ML = 4.4) in ESZ, from [38] and the respective epicenters (yellow stars). Dashed in black (Lower Tagus Basin).

North of Arraiolos, the relief is marked by the escarpment of Santana do Campo, of a tectonic nature. This escarpment establishes the passage from the high level of the Évora peneplain (300–340 m) to the compartment where the Divor river flows (240–250 m), whose surface slopes towards the lower Tagus basin [42,43]. To the west, there is the Sabugueiro tectonic ditch, which is a depression with a flat bottom at a 200 m altitude, bordered on the SW side by a granite fault escarpment [44] that is part of the Vimieiro granitic massif. This morphotectonic element is associated with the Ciborro fault, which extends SE to the locality of Gafanhoeira and gives rise to an 80 m gap between the bottom of the Sabugueiro depression and the flap of the Semper-Noiva applanation [43]. The mountainous area of Aldeia da Serra ends at N by a step of about 100 m due to an oriented fault E–W (Lineament of S. Gregório), while the southern slope descends more smoothly [39].

The Ciborro Fault and the Lineament of São Gregório have been associated with earthquake alignments with the same direction [1,2,8,9]. Field geology studies [8] along the Ciborro Fault showed granites riding sediments from the Coruche Argillaceous-Gross Complex, considered to be of the Mio-Pliocene age. The fault separating these two geological units has a N80°W attitude, 80S, and shows kinematic evidence of having a thrust component to the northern quadrant, placing the Paleozoic granites on the Tertiary sediments [8]. The outcrop is located exactly at the base of the geomorphological step associated with the Ciborro Fault.
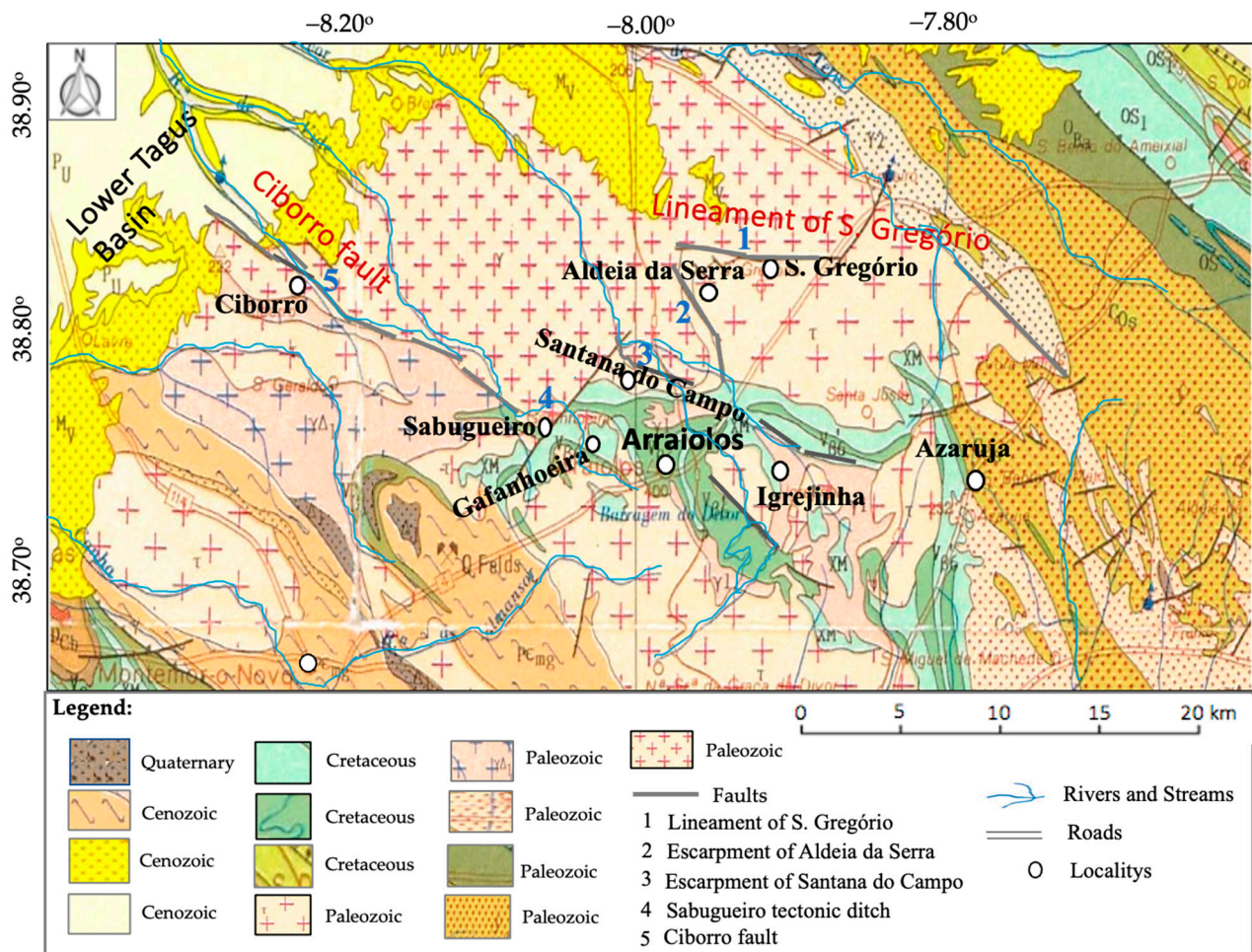
Figure 2. Excerpt from the geological map of the study region (adapted from the geological map of Portugal at scale 1:500,000. The main tectonic accidents are also represented, namely: the Lineament of São Gregório and the Ciborro fault, the escarpments of Aldeia da Serra and Santana do Campo, respectively. Adapted from [41].

3. Temporary Seismic Network and Data

The present study uses seismological data from a total of 37 seismic stations installed as permanent and temporary installations in the Arraiolos region (Figure 3). In order to monitor the seismic sequence of the Arraiolos earthquake of 15 January 2018, the ICT, in partnership with the IDL, 1 h 30 min after the main shock, proceeded to install 12 broadband stations, equipped with Guralp CMG-6TD sensors, consisting of an integrated system with three components of broadband sensors with a flat response between 0.033 Hz and 50 Hz, a high dynamic digital register (24-bit), and 21 short-period stations, equipped with a CDJ-S2C-3 sensor, with a natural frequency of 2.0 Hz, totaling 33 stations, operating in continuous mode at a sampling rate of 200 Hz per second for the three components of each station and with hourly synchronization by GPS (Global Positioning System). This network was called the Arraiolos temporary seismographic network. With the three permanent stations of the national network (IPMA) and ICT, and a permanent station installed by the IST (Instituto Superior Técnico), 37 seismic stations were added, distributed in a radius of approximately 30 km around the epicenter of the main shock (Figure 3). The seismic network recorded the local seismicity with local magnitudes ranging between $-0.9 < ML < 4.9$.
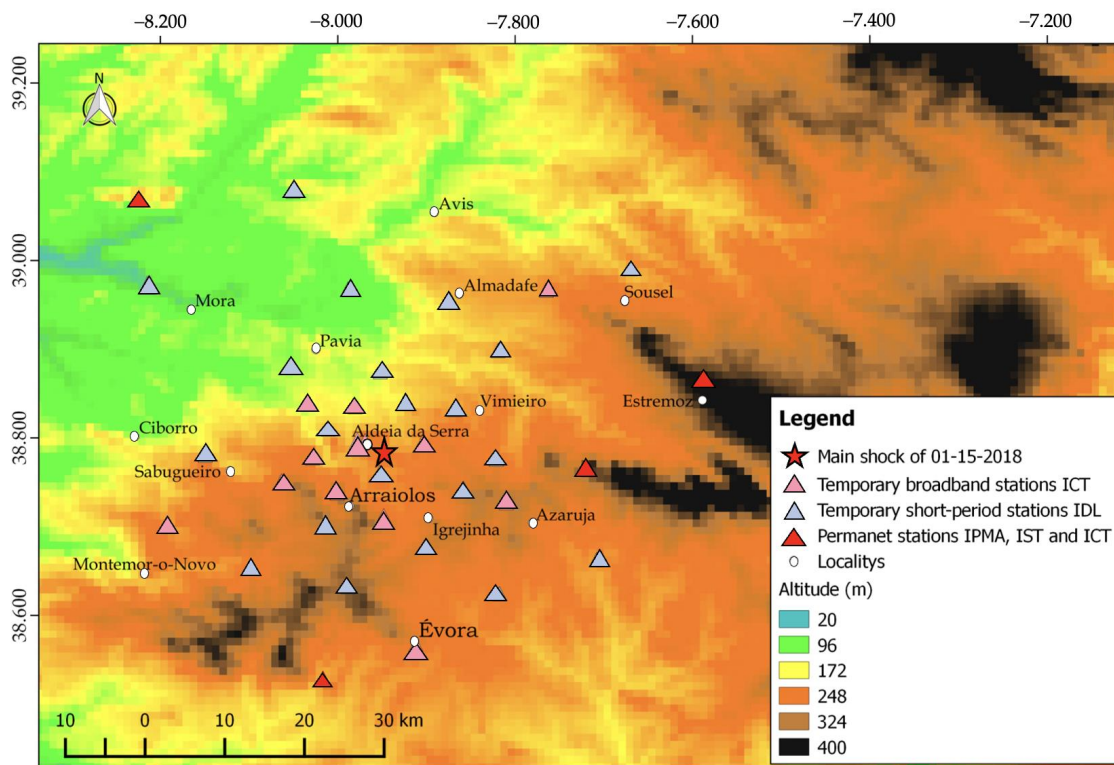
Figure 3. Distribution of stations in the temporary seismic network of Arraiolos (blue triangles and rose) around the epicentral zone of Aldeia da Serra, installed after the Arraiolos earthquake of 15 January. Red triangles: permanent seismic stations of IPMA (Instituto Português do Mar e da Atmosfera), IST (Instituto Superior Técnico), and ICT (Instituto de Ciências da Terra). The data recorded by these stations were used in this study.

Figure 3 shows the distribution of stations in the temporary seismic network of Arraiolos, the permanent seismic stations of IPMA, and the accelerograph of the IST (Instituto Superior Técnico) used in this study. The introduction of this temporary network of Arraiolos resulted in obtaining a greater number of seismological data and lowering the magnitude threshold, resulting in a better characterization of the seismicity and focal mechanisms of this region.

During the seismic monitoring period (15 January–30 June 2018), a total of 466 events identified as having a number of phases suitable for their location and further analysis were detected. The detection of seismic events was done manually through the inspection of daily spectrograms of the set of stations in operation (carried out in collaboration with the IDL). These seismological data were analyzed by SEISAN version 10.3 [45]. We considered 389 well-located earthquakes, having an average root mean square (RMS) travel time error ≤ 1.0 s and an azimuthal gap smaller than 180°, with minimum 6 P and 6 S phase readings.

The localization of the Arraiolos seismic sequence was done using the Hypocenter program [46–48] incorporated in the SEISAN software package (Version 10.3). The hypocenter implements the Geiger method, which uses a linearized least squares approach to solve the inverse problem of finding the earthquake's hypocenter and origin time, given the arrival times of different seismic phases at different recording stations.

Considering the geological heterogeneity in mainland Portugal and the distribution of seismicity, it is necessary to find a specific velocity model for each region, followed by a final inversion using the data selection that results in the best 1-D minimum model (Figure 4) with the VELEST inversion [49] that fits the observations. The inversion criteria and procedures can also be consulted in the work of Dias [50] which highlights several initial models and inversion models. In this study, a 1D velocity model was used, assuming a Vp/Vs ratio of 1.74, based on the 3D tomographic model by [51], after an adjustment of

the Vp/Vs ratio determined by the data, which went from 1.70 to 1.74 (Figure 4), where Vp and Vs are the velocity of the P and S waves in the middle, respectively.
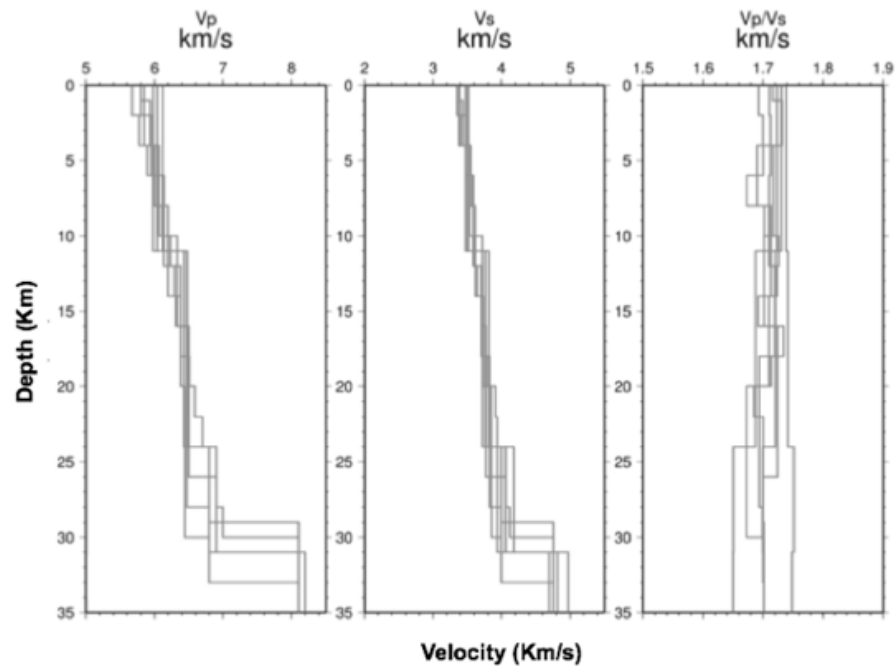

Figure 4. D velocity model of P and S waves, obtained with VELEST inversion.

Phase picking was performed for the P (recorded in the Z component) and S (recorded in the E or N component) waveforms. The localization program calculates the azimuth (azm), angle of incidence (ain), the epicentral distance and the residuals of arrival times. The temporal residuals of the observations of the seismic phases (P and S) as a function of distance are illustrated in Figure 5.
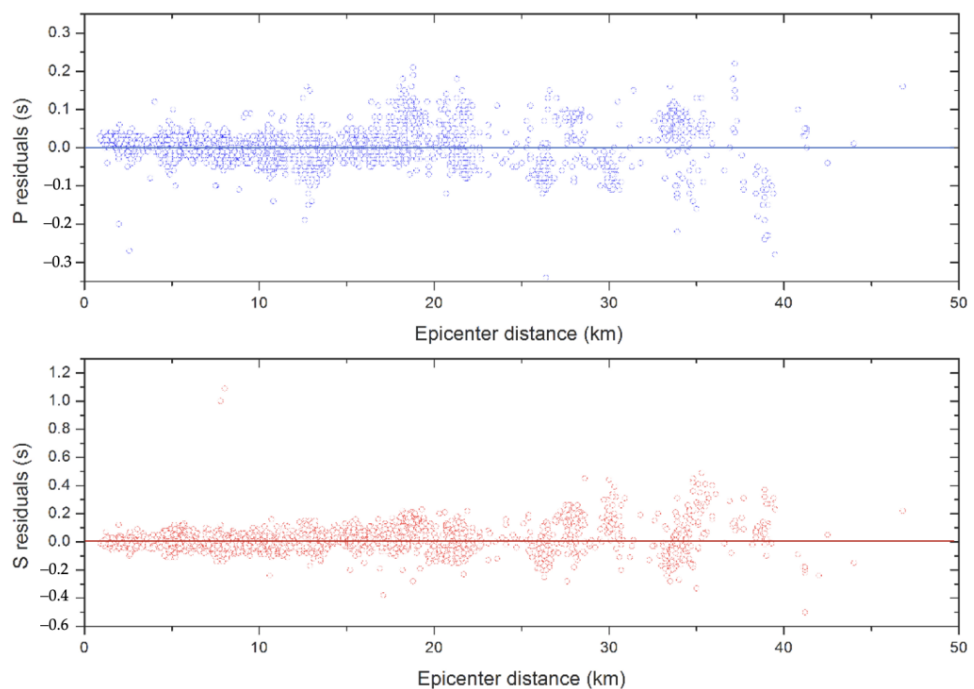

Figure 5. Temporal residuals of seismic phase observations (RMS) as a function of distance. Above: P phase; below: phase S. Red circles—S phase residuals. Blue circles—P phase residuals. The red and blue lines mark the zero-level residuals.

In fact, the smaller the epicentral distance, the lower the RMS will be. It is notorious that the P phase has lower residual values, with values between −0.1 and 0.1 s. Between 18 and 37 km there are some peaks with RMS values between 0.1 and 0.2 s, and between 33 and 40 km there are some peaks with values below −0.1 s. In the case of the S wave, there is some symmetry in the residuals, with values between −0.2 and 0.2 s, except between 27 and 40 km of epicentral distance, whose values tend to exceed 0.2 s, reflecting the greater difficulty in marking this phase, that is, the presence of higher residues with greater deviations in the S phase relative to the P phase is justified by the fact that it is a phase whose reading is subject to greater error due to the overlap with the P wave coda and the S wave window. In general, in both cases, the RMS values are considered low, revealing that there are no gross errors in the marking of the seismic phases.

4. Spatial and Temporal Character of the 15 January 2018 Earthquake Sequence

4.1. Spatial-Temporal Distribution of Aftershocks

A detailed analysis was carried out on the seismic sequence started on 15 January 2018 (see Figure 6a), which produced about 466 events until 30 June 2018, detected by the temporary seismographic network of Arraiolos, in which about 318 events (68%) were registered by the end of February.
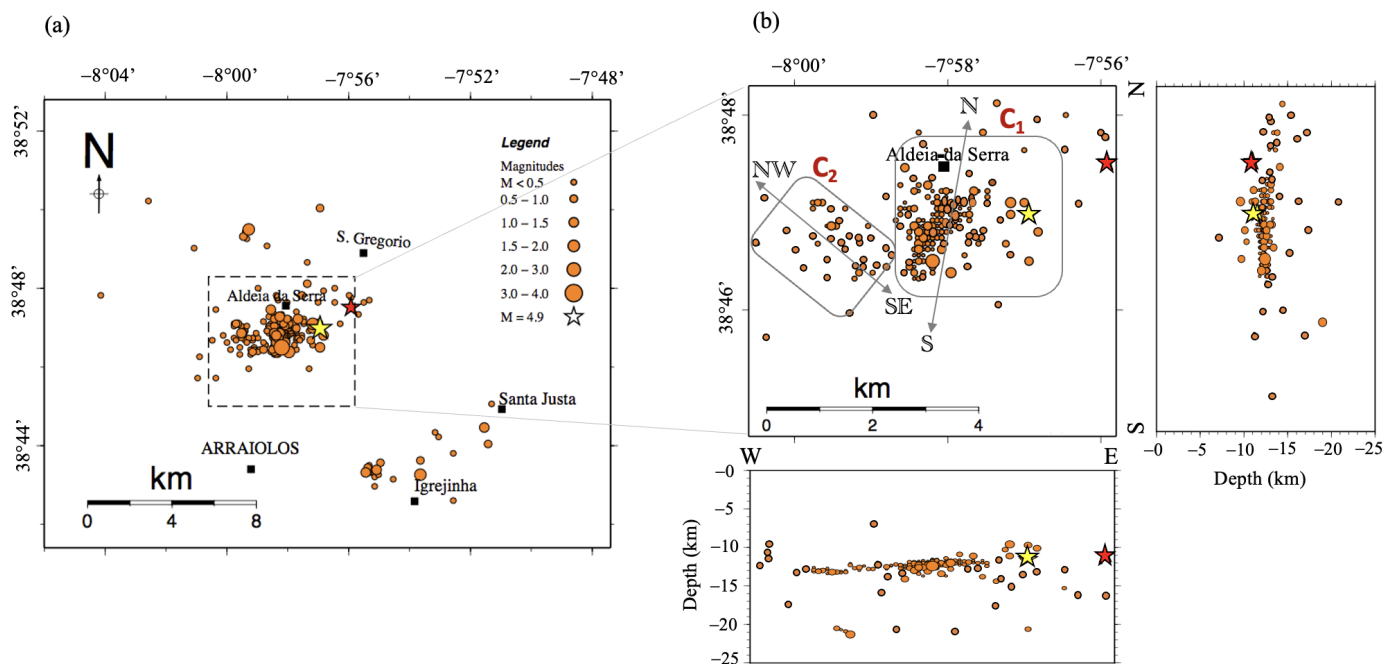

Figure 6. (**a**) Epicentral distribution of the 2018 Arraiolos seismic sequence (15 January–30 June 2018). Epicentral location of the main earthquake determined by IPMA (red star). Relocation of the main shock determined in this study (yellow star) and the spatial distribution of the epicenters of the 2018 seismic sequence analyzed in this work (389 events with a GAP < 180°). (**b**) Epicentral distribution of the seismic sequence in a more restricted zone (Aldeia da Serra) in figure (**a**), and the vertical distribution of hypocenters in two profiles, according to the E–W and N–S directions, centered at 38°45′N and 38°48′N, and by the longitudes 7°56′W and 8°06′W. Identification of two clusters of events, namely: Cluster 1 (C1): I gathered 2/3 of the events, with N–S and NW–SE guidelines. Cluster 2 (C2) events oriented in the NW–SE direction.

In this work, we seek to relocate the main earthquake of 15 January 2018, using a 1-D velocity model (Figure 4) adjusted and adopted for the study region, as well as the inclusion of seismological data from the two closest stations to the epicenter (VERN and EVMO, respectively), whose seismic phase readings contributed to the reduction of the RMS (which went from 0.4 s to 0.3 s).

Figure 6 represents the distribution of the epicenters of the 389 events studied (with a GAP < 180°), as well as two depth profiles according to the WE and SN directions, and the relocation of the main shock determined in this study that places the epicenter of the aftershocks closer, compared with the location determined by the IPMA, with an epicentral difference of approximately 2 km, with a slight change in the focal depth, from 11 km to ~12 km, where the majority of the aftershocks are concentrated, revealing that the largest Seismic activity recorded in 2018 by the temporary seismographic network in the region of Arraiolos occurred in Aldeia da Serra, and a smaller agglomerate recorded in the area of Igrejinha-Azaruja. This epicentral distribution shows that there is greater organization in the arrangement of the epicenters, which tend to group themselves into two clusters of events in the Aldeia da Serra zone, one of them gathering around 2/3 of the microseisms (see Figure 6a). The depth distribution of the two profiles reveals a greater concentration of events at ~12 km (Figure 6b), indicating that the fragile layer will be confined to the most superficial 12–13 km of the lithosphere.

The observation of Figure 7a reveals that there is some definition in the possible alignments of seismicity, with the existing geological faults. The N–S and NW–SE alignment of the event cluster of Aldeia da Serra appears to favor the hypothesis of [8], of moderate-to-weak neotectonic activity along the Ciborro Fault and the Lineament of S. Gregório. According to these authors, these faults are responsible for the genesis of the Aldeia da Serra relief (Figure 7c).
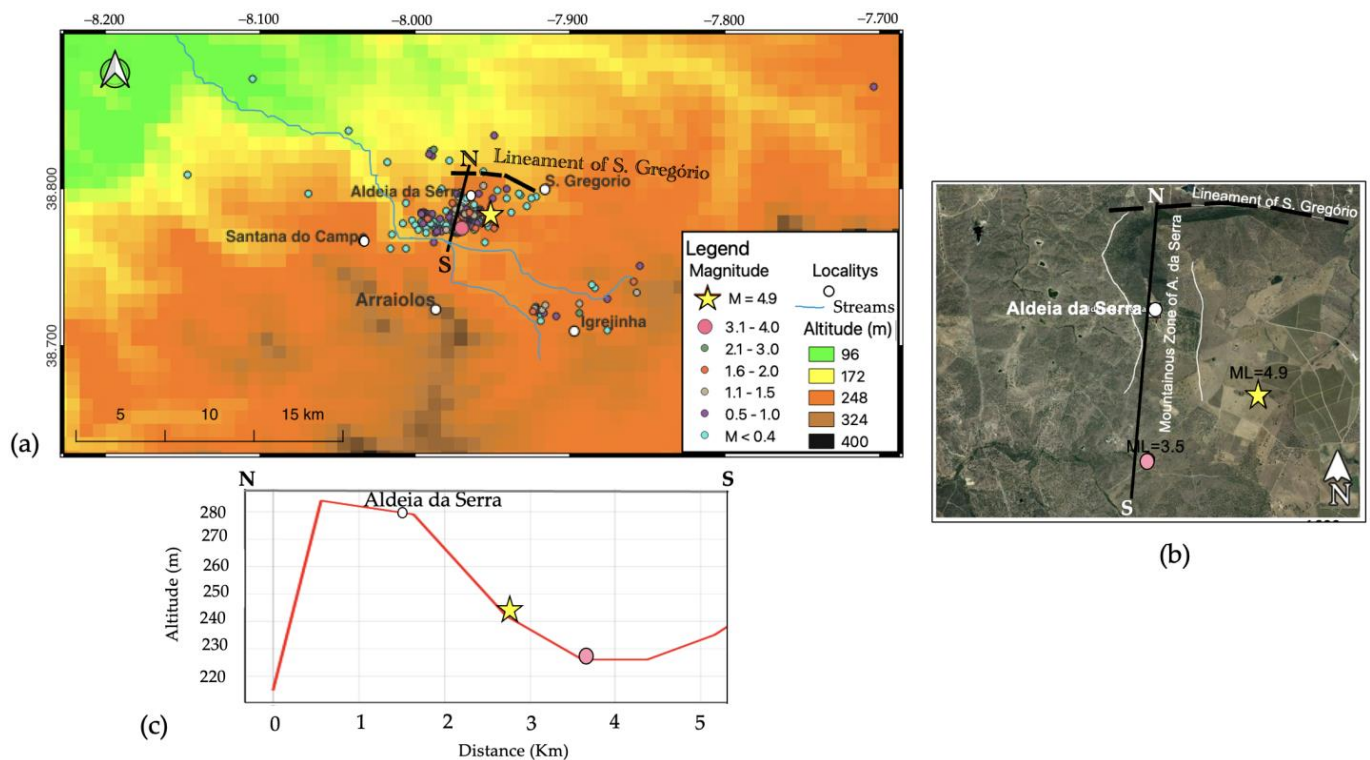

Figure 7. (**a**) Epicentral distribution of aftershocks in the Aldeia da Serra area. Dashed line illustrates the Lineament of São Gregório (WNW–ESSE direction); the line N–S indicates the elevation profile of Aldeia da Serra, represented in (**c**). (**b**) Satellite image of the Aldeia da Serra area, where the mountainous area of Aldeia da Serra can be observed, oriented in the N–S direction, which tends to coincide with the orientation of the largest seismic cluster recorded, concentrated on the southern flank of this mountainous area. The two largest seismic events of 2018 are also represented: yellow star—main earthquake (ML = 4.9), pink circle—aftershock with the highest recorded magnitude (ML = 3.5). (**c**) Topographic profile of the Aldeia da Serra Escarpment (N–S direction).

The observations in Figure 7a–c seem to reveal that the mountainous area of Aldeia da Serra, oriented in the N–S direction, which tends to coincide with the orientation of the largest seismic cluster recorded, concentrated on the southern flank of this mountainous area, would correspond to the possible nucleation point of seismicity and where the main earthquake of 15 January 2018 would have originated.

Here, we also investigate the spatial distribution of seismicity over time (1961–2018) in order to identify the ASZ seismogenic sub-zones. For this purpose, we have included all events recorded by the national IPMA network in the period 1961–2018, and the 466 events recorded by the 2018 temporary seismographic network of Arraiolos.

A general look at Figure 8 shows that the seismicity of the Arraiolos Seismic Zone (ASZ) is oriented in the NW–SE directions, where it is possible to identify three seismogenic sub-zones, namely: the Ciborro Seismic Zone (CSZ), the Seismic Zone of Aldeia da Serra (ASSZ), and the Seismic Zone of Igrejinha-Azaruja (IASZ). The ASZ seismicity distribution (1961–2018) reveals that the highest concentration of earthquakes occurs between latitudes 38°49′N and 38°45′N and longitudes 8°05′W and 7°70′W in the seismic zone of Aldeia da Serra (ASSZ). This means that the seismic activity of this zone, despite its low magnitude, is significant in the regional context.
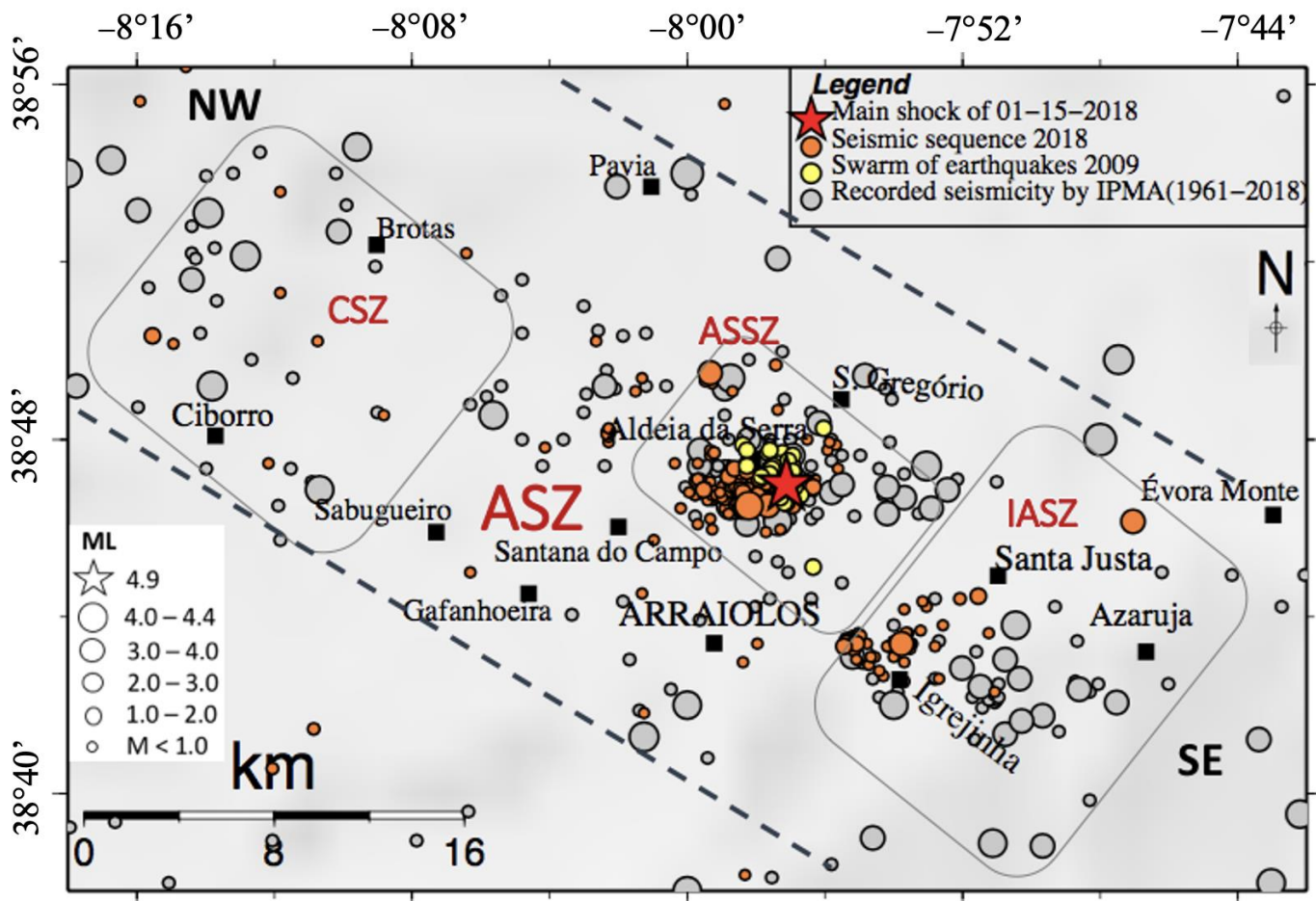

Figure 8. Spatial distribution of earthquakes in the Arraiolos Seismic Zone (ASZ) according to NW–SE directions, recorded in the period 1961–2018, and the identification of the 3 seismic sub-zones defined in this study. Location of the earthquake of 15 January 2018 (red star) and its seismic sequence analyzed in the period 15 January–30 June 2018 (466 events with GAP < 360) (orange circles) recorded by the temporary seismic network of Arraiolos, being the locations of the 2009 seismic swarm (yellow circles) in the Seismic Zone of Aldeia da Serra and the locations of the earthquakes (grey circles) recorded by IPMA national network (1961–2018) are also represented.

The earthquakes in CSZ have an average depth of 15.0 km and average magnitudes (ML = 1.5), and in IASZ they have an average focal depth of 15.5 km and average magnitudes (ML = 1.3). The ASSZ earthquakes are more numerous and have an average depth of 12.0 km and magnitudes of $-0.9 < ML < 5.0$. This zone (ASSZ) is also characterized by the occurrence of seismic crises, such as the seismic crisis that occurred on the 16th and 17th of June 2009, having registered 41 earthquakes of low magnitude ($0.6 \leq ML \leq 2.0$), located at a depth between 1 and 11 km (Figure 8, yellow circles), denoting a unique seismic behavior in this region. The sequence of these seismic events is not associated with any main event and, therefore, they are classified as "swarm", according to the criteria of Mogi [52].

The temporal distribution of seismicity in the ASZ region during the period 1961–2018, shown in Figure 9, confirms that the Arraiolos earthquake of 15 January 2018 is the largest instrumental event recorded in that area. From this figure it is easy to see that there is a progressive increase in the number of earthquakes, which corresponds to the improvement of the observation network with the consequent detection of earthquakes of decreasing magnitude.
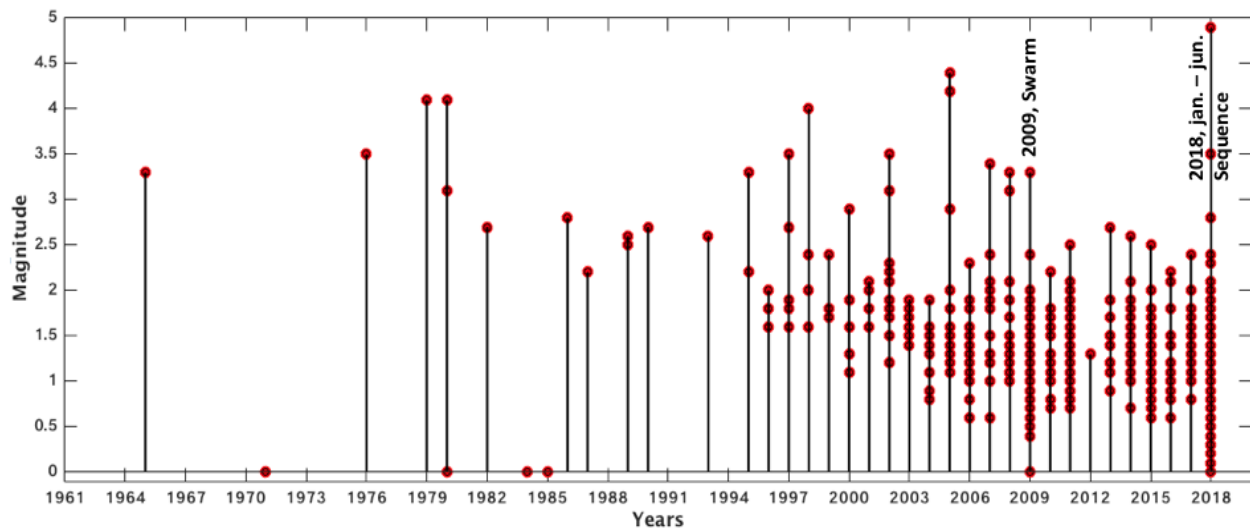

Figure 9. The time distribution of the seismicity (ML $\geq$ 0) of the ASZ region during the period 1961–2018.

The temporal distribution of the seismic sequence which started on 15 January 2018 was also analyzed. In Figure 10, the temporal distribution of this sequence is illustrated. During the first 10 days of the crisis, after the main shock, there was a significant increase in events. From the 11th to the 24th day, there was a reduction in the number of events. At the end of the 24th day, it was verified that the seismic sequence had been rejuvenated (Figure 10a,b). We can see a great irregularity with the possible renewal of the crisis on the 26th, where nine events were registered.

This rejuvenation does not coincide with the occurrence of an earthquake of greater magnitude, as shown in Figure 10b (illustrated above), which illustrates the evolution of the seismic sequence as a function of magnitude and time elapsed from the moment of origin of the main shock. The origin of this rejuvenation may be due to a delayed response to stress build-up due to the first phase of the seismic sequence. Therefore, this statement is not conclusive, so it is necessary to seek further scientific explanation. After 26 February to 30 June (~125 days) the seismic activity became stationary, with an average of ~1 event per day, reaching certain magnitudes ($-0.3 \leq ML \leq 2.8$). During this period, the temporary seismic network was reduced by 12 to 6 stations, respectively.
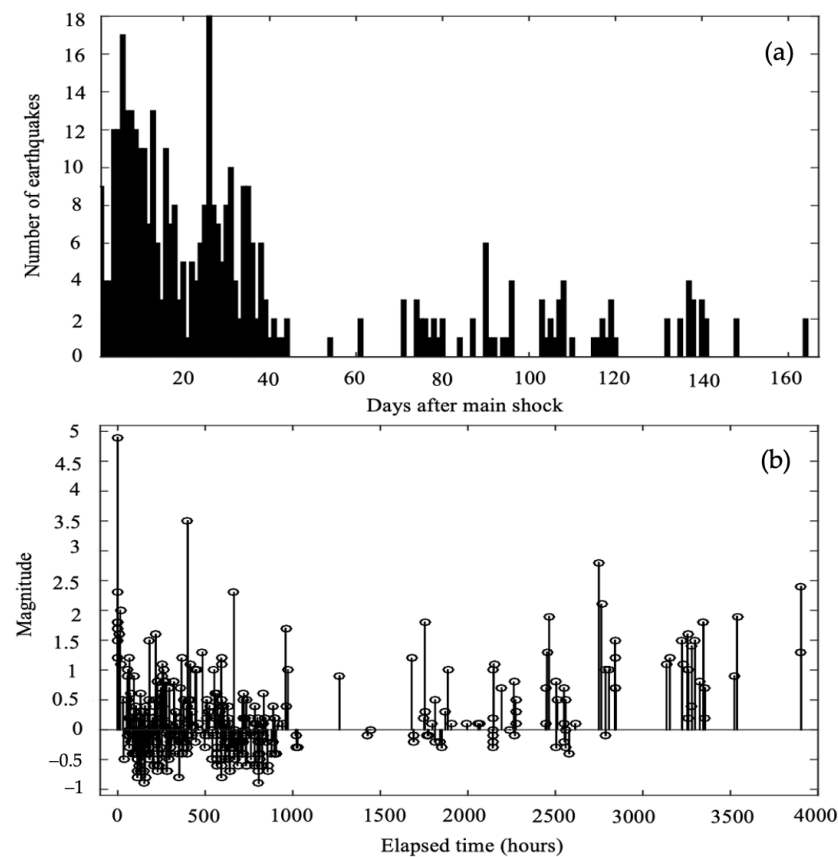
Figure 10. Temporal distribution of earthquakes (15 January–30 June 2018). (**a**) Daily number of events after main shock. (**b**) Evolution of the seismic sequence, from the time of origin of the main shock.

Normally, after a main shock, the magnitude and frequency of minor tremors follow characteristic distributions known as Gutenberg–Richter and Omori laws, respectively. Considering the variation in the detectability of the seismographic network during the recording period, as shown in Figure 11a, in this work, it was not possible to calculate the parameters of Omori's law, which recommends a well-recorded sequence from the main shock [53]. On the other hand, the Gutenberg–Richter (GR) law [54] describes the expected number of earthquakes per unit of time as a function of magnitude, as shown in Equation (1):

$$\mathrm{Log}N(M) = a - bM. \tag{1}$$

where $N(M)$ is the cumulative number of events during a given time interval with magnitudes equal to or larger than M, and a and b are constants that may vary in space and time. The parameter a characterizes the overall productivity of seismic activity in a given area during the study period. The b-value of the Gutenberg–Richter law evaluates the ratio of low-magnitude to high-magnitude earthquakes. This b-value undergoes spatial and temporal variations due to many factors, such as crustal heterogeneity [52], the stress level imposed on rocks [55,56], pore pressure, geothermal gradient [57], and, in some cases, data from incomplete catalogs and the calculation method can also cause changes in b-values [58]. Regions where earthquakes result from tectonic stresses typically exhibit values of b~1 [58–60]. High values of b usually result from failures associated with pore pressure changes, e.g., [61], and tend to occur near active magma chambers [62,63], subduction zones [64,65], and sites of induced seismicity [61].
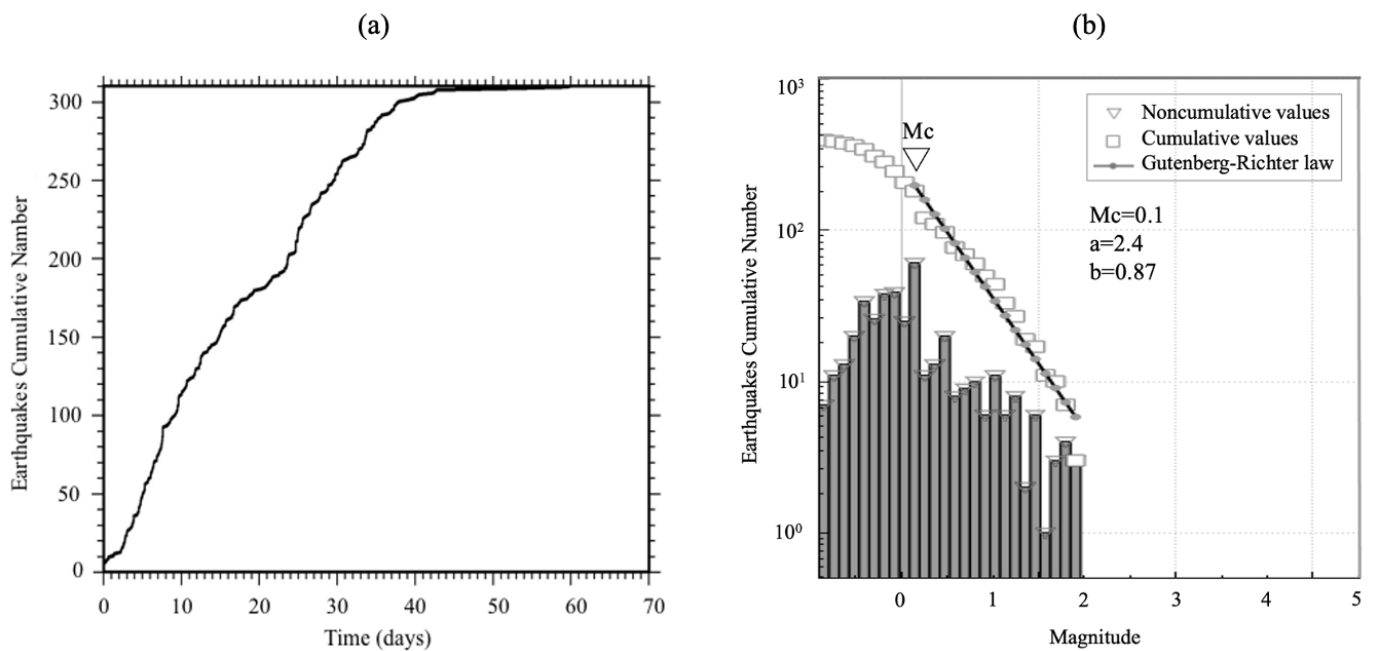
Figure 11. Temporal distribution of earthquakes (15 January–30 June 2018). (**a**) Cumulative numbers of observed aftershocks of 2018 Arraiolos earthquake versus time (in days) elapsed from the main shock. (**b**) Cumulative and non-cumulative numbers of observed earthquake magnitudes in 2018 seismic Arraiolos sequence. The blue triangle is the magnitude completeness. Fitted Gutenberg–Richter law to the observations along with the estimated parameters are also shown.

To analyze the *b*-value, one must understand that the linearity relation between log*N* and *M* of the law of recurrence GR holds only for magnitudes of a certain interval. In this sense, we calculate the *b*-value using the function 'Gutenberg–Richter Relation' that allows one to determine the *a* and *b* values for a given catalog using different magnitude intervals and bin sizes. To obtain a more stable solution (good linear fit), the maximum magnitude was considered in the regression (ML < 2.0), removing from the catalog the events with the highest magnitudes, about six events ($2.0 \leq ML \leq 4.9$), since the number of earthquakes at larger magnitudes fell quickly below the GR line, meeting the limited period of observation, the result of which is shown in Figure 11b. It appears that the distribution of the accumulated number of events as a function of magnitude follows the Gutenberg–Richter law with a *b*-value equal to 0.87 (approximately 1), which suggests a tectonic origin for the earthquakes in the region, indicating a proportionally higher number of small earthquakes compared to those of greater magnitude (ML > 2.0).

5. Focal Mechanism Determination

5.1. Method

Many methods can be used to compute focal mechanisms: using initial polarity of the P wave, e.g., [66], or the P and S waves, e.g., [67]; spectral amplitudes combined with P-wave polarities, e.g., [68]; S/P-wave amplitude ratios, e.g., [23,69,70]; or inversion of full waveforms, e.g., [71–73]. The method chosen typically depends on data availability and project goals.

In this study, we apply the HASH program developed by Hardebeck and Shearer [21]. This program calculates focal mechanisms from first-motion P-wave polarity observations. The principle of this method consists of calculating a set of acceptable fault plane solutions that fit the phase data within a predefined misfit limit and returning to the preferred solution as the mean of this set (Figure 12). The HASH algorithm determines the quality of the focal mechanism based on the robustness of the solution against variations in the model of seismic velocity, earthquake depth, and random polarity errors [22]. This program

requires, as input, the azimuth and angle of the seismic ray to each station as it leaves the seismic source, velocity models, and the first-motion polarity of the P-wave recorded at the station, and calculates different take-off angles for the rays traveling to each of the seismic stations.
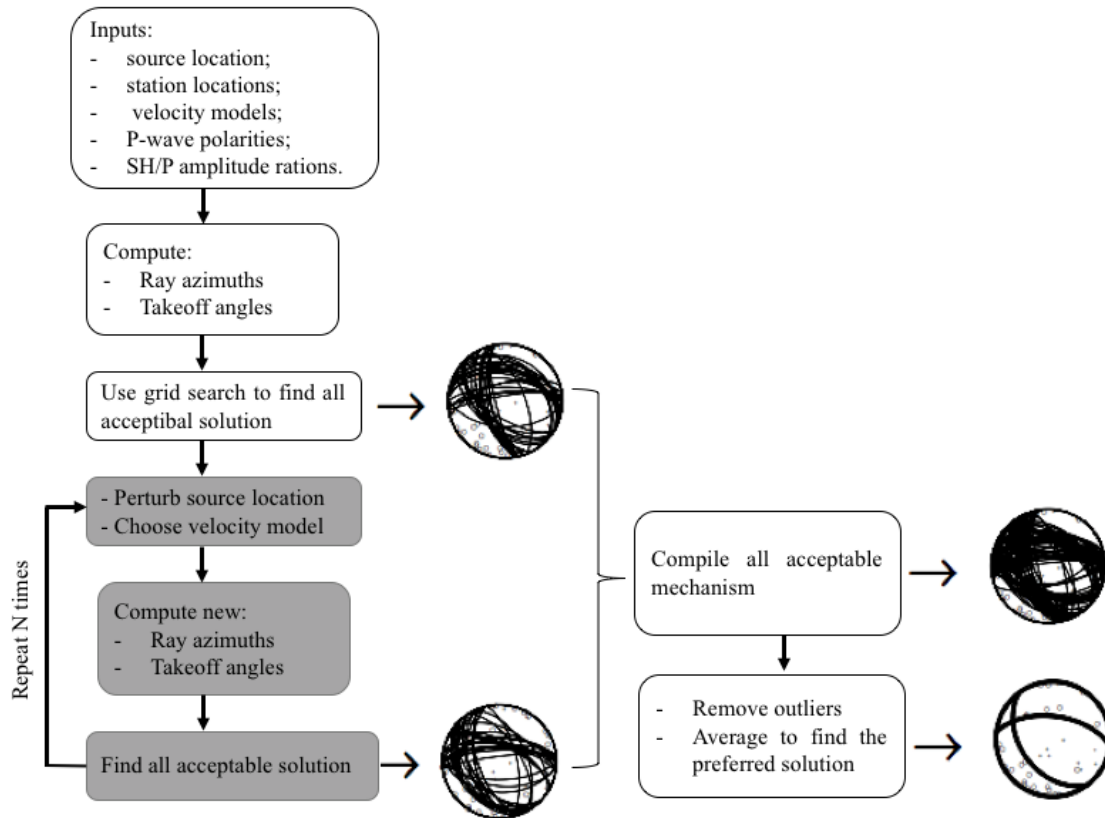

Figure 12. Flowchart of the method used for determining earthquake focal mechanisms in this study.

The final HASH quality grade (HASH-Q) is based on the stability of the solution, quantified as the fault plane uncertainty (FPU), the fraction of misadjusted polarities, and the station distribution rate (STDR). The Fault Plane Uncertainty Parameter is the best discriminator of the HASH program, depending on the number of observations per event, that is, first-motion polarities and S/P amplitude ratios. The good azimuthal coverage of the observation stations is an important factor in the quality of the focal mechanisms obtained from the first movement polarities of the P wave [74]. This technique has shown the ability to produce more robust focal solutions for cases where the correct mechanisms are believed to be known [22,23,75]. Hardebeck and Shearer [23] updated the HASH algorithm including S/P amplitude ratios and showed that they can be useful for constraining the focal mechanisms of small earthquakes. The principle of the amplitude ratio method consists in canceling the effect of geometric scattering (propagation effects) by forming the amplitude proportions of S and P waves (e.g., SH/P) of the same type of phase, Pg and Sg. The P wave amplitude is defined by the peak value of the vertical component, and the S wave amplitude is measured as the vector sum of the radial and vertical components. In this study, we use only SH/P amplitude observations. Amplitude ratio observations were corrected for site and path effects, following the approach of [23] for all seismic stations.

Regarding the selection of the ideal parameters for the HASH program, we tried to test the robustness of the result in relation to each input, in order to obtain more robust solutions. After testing, some default values provided by the HASH program were kept. For focal mechanisms, we selected estimated earthquakes with a magnitude range of 1.0–4.9. Only focal mechanisms estimated with eight or more P-wave polarities and six or more read of phases, GAP < 180°, minimum number of amplitude ratios was three, and the error in

amplitude ratio was in the range of 0.02–0.2. We computed 54 mechanisms for the same set of 466 located earthquakes and a number of the mechanisms' quality parameters (see in Section 5.2). Figure 12 shows a typical example of a focal mechanism, with the solution obtained using the current method.

5.2. Results

The focal mechanisms make it possible to identify, in each region, the pattern of current tectonic movement, enabling correlations between this type of geophysical information and geological data.

The preferred solution is found to be the average of the acceptable solutions of the fault plane after removing the extreme values. This method provides the focal mechanism parameters, strike ($\varnothing°$), dip ($\delta°$), and rake ($\lambda°$), for one of the two planes of each mechanism, as well as the error estimates.

For the 54 seismic events chosen, we determined (see Table A1 in Appendix A) the solutions of the focal mechanisms (strike, dip, rake), the origin time, the location and magnitude of the event, the estimation of the uncertainties of the fault planes (FPU), the station distribution rate (STDR), the weighted fraction of polarity misfit (Fσ), the number of polarities, the SH/P amplitude ratio error, and the quality of the focal mechanism solution based on the criterion proposed by Hardebeck and Shearer [21].

The FPU decreases with the number of observations per event, that is, the first movement polarities and S/P amplitude ratios [20]. The additional data of the S/P amplitude ratios allowed us to improve the precision of the focal mechanisms, significantly decreasing the mean nodal plane uncertainties compared to the mechanisms that include only the P wave polarities, as illustrated in Figure 13.
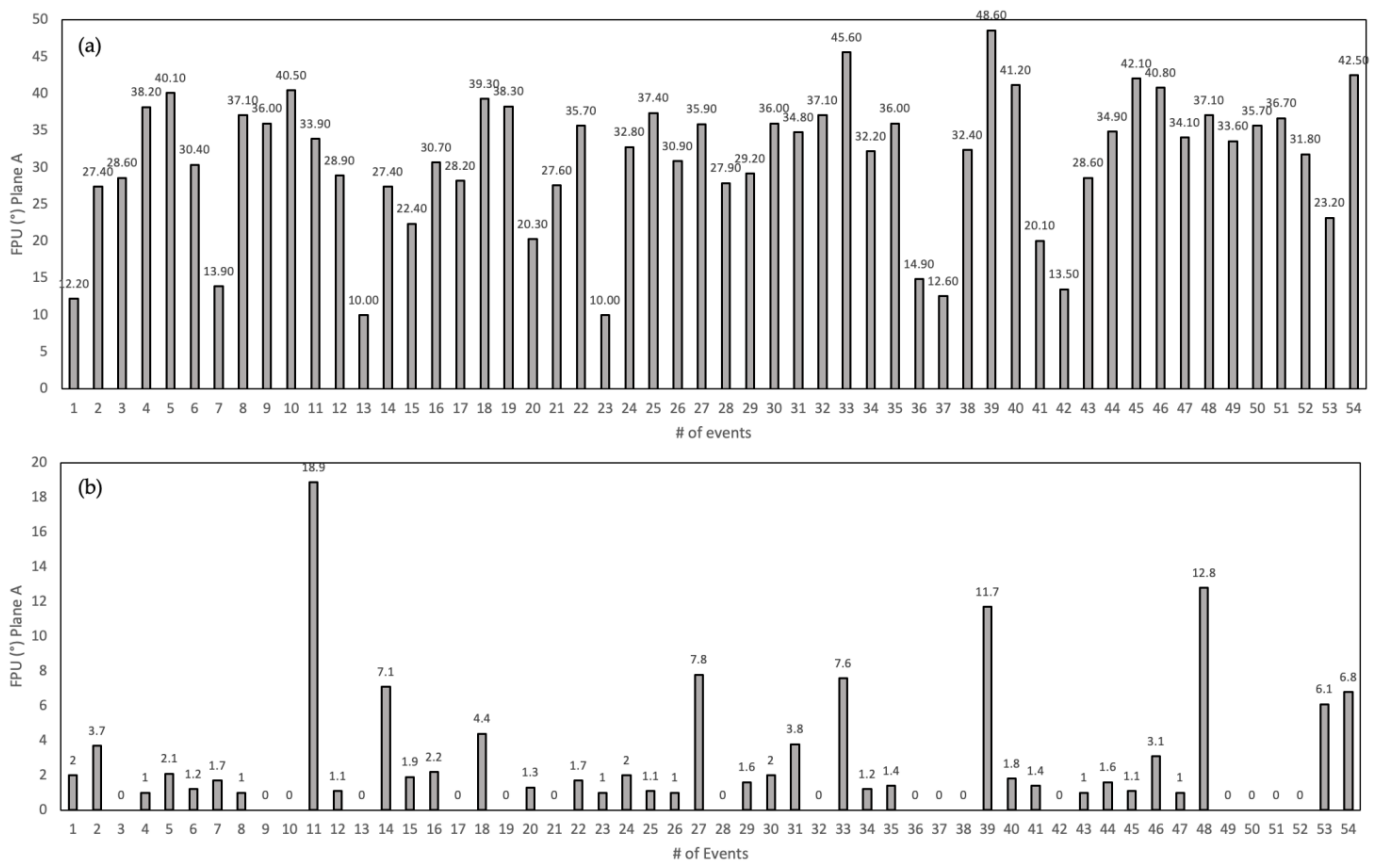

Figure 13. Estimation of uncertainty of failure plans (FPU). Example: plan A, for the solutions of the focal mechanisms of the 54 events studied, initially calculated through the polarities of the first P wave arrival movement (**a**), and the additional data of the SH/P amplitude ratios (**b**).

Nodal plane errors are defined as 1 sigma fault plane uncertainties, defined as the Root-Mean-Square (RMS) angular difference of the preferred plane's acceptable fault planes, and range from 0° to 90°. Only if the RMS angular difference between the acceptable mechanisms and the preferred mechanism is less than 35° is a solution considered to be suitably stable. In this study, RMS values ≤35° were obtained. The station distribution rate (STDR) represents the distribution of the first movement data in the focal sphere in relation to the radiation pattern, and the observations are closer to the nodal planes for smaller values of STDR. It ranges from 0 to 1, with larger values showing more robust solutions (>0.50). The values obtained from STDR are >0.50, except for one event, which means that most of the data are far from the nodal planes. Although solutions with low ratios (e.g., <0.5) are expected to be less robust than those with high values [66], there is no obvious relationship to FPU. The fraction of misadjusted polarities also contributes to the uncertainty of the mechanism, where 0.0 is a perfect fit and 1.0 would be a perfect misfit. In all cases the values obtained are ≤0.16, which indicates mechanisms with good fits. All the solutions of the focal mechanisms of the events determined in this study are shown in Table A1 (in Appendix A).

Figures 14 and 15 represent the distribution of the P-wave polarities of the selected events, which illustrates a more or less uniform distribution over the focal sphere for most mechanisms, due to the good spatial coverage of the seismic stations. The classification scheme proposed by Hardebeck and Shearer [21], shown in Table 2, is used to characterize the quality of the obtained focal mechanisms. This classification suggests that mechanisms of type A, B, and C are, in general, reliable solutions. Of the focal mechanisms obtained, 94.44% (51 mechanisms) correspond to class A and only 5.56% (three mechanisms) to class B, respectively.
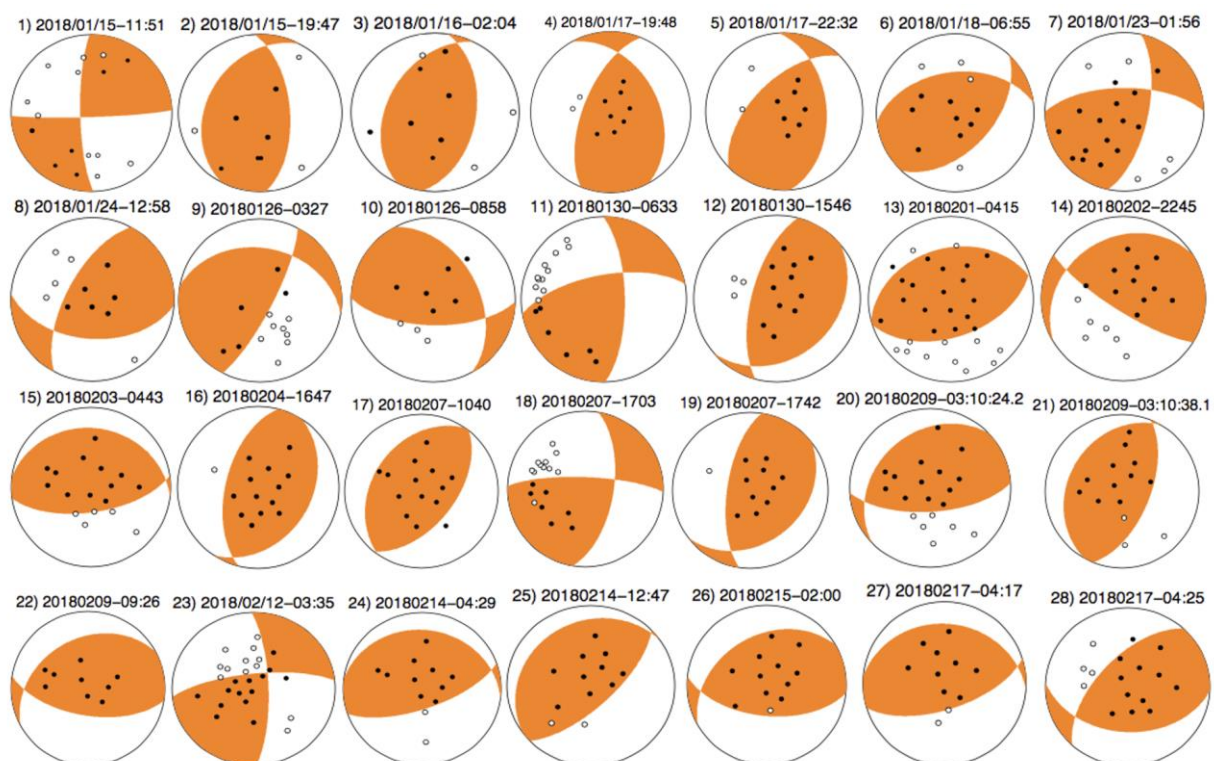
Figure 14. Solutions of the focal mechanisms of the studied events (1 to 28 of Table A1 in Appendix A), through the P wave polarities and SH/P amplitude ratios, selected in the period from 15th January to 30th June 2018, which occurred in the study region. The polarities of the P wave are represented on the focal sphere with indication of the compression quadrants, which correspond to the tension axes T (black circles) and the dilation quadrants, which correspond to the compression axes P (white circles), respectively.
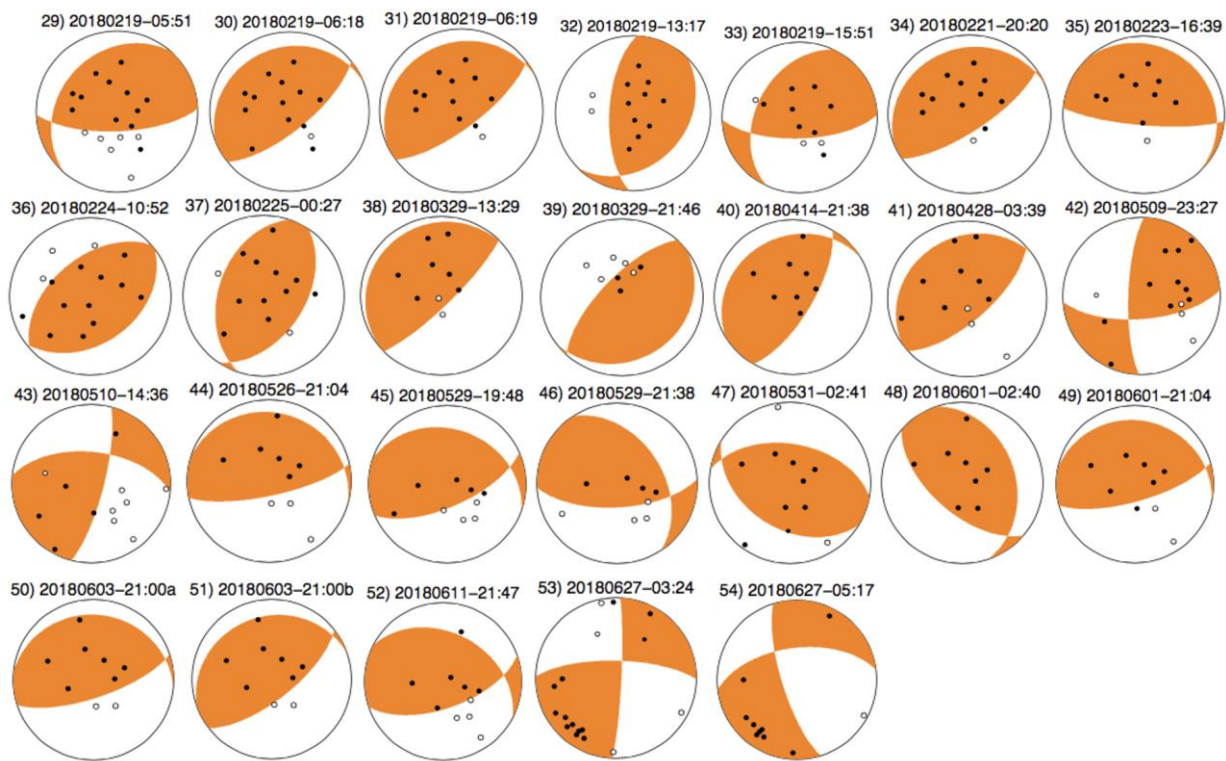
Figure 15. (Continuation). Solutions of the focal mechanisms of the studied events (29 to 54 of Table A1 in Appendix A).

Table 2. Focal Mechanism quality criteria used in this study [20] and Number of Events for Each Defined Quality.

Quality (Q_HASH)	Average Misfit	RMS Fault Plane Uncertainty (°)	Station Distribution Ratio	Mechanism Probability (Percent)	N° of Events	%
A	≤0.15	≤25	≥0.5	≥80	51	94.44
B	≤0.20	≤35	≥0.4	≥60	3	5.56
C	≤0.30	≤45	≥0.3	≥50	-	-
D			All the rest			
Total					54	100

Most events are predominantly of the reverse type, with planes oriented in the NNE–SSW direction and others in the WNW–ESSE direction, and a minority of strike-slip type fault events, with planes oriented in the N–S and E–W direction, respectively. In general, the orientation of the P and T axes of the seismic sequence events are consistent with the main shock solution, with the P axes of a NW–SE trend. The T axis orientations spread around an NNE–SSW oriented band. This pattern of focal earthquake mechanisms reflects a stress system characterized by uniaxial compression, which is called horizontal compression when oriented in the NW–SE direction. This orientation agrees with the stress field expected in the area [1,2,76].

Figure 16 illustrates the general map of the focal mechanisms of the events of the Arraiolos seismic sequence, determined in this study (Table A1 in Appendix A), and the triangular classification diagram of the focal mechanisms with different colors that correspond to different types of faults according to the standard classification [76]. In these mechanisms, two main groups can be distinguished. The first one corresponds to strike-slip shutdown events, where the main shock (M = 4.9) that occurred on 15 January 2018 is found with the other aftershocks. The second group corresponds to the predominant focal mechanisms of the seismic sequence, which are of the reverse fault type, which contrasts with the

focal mechanism of the main shock (strike-slip type). Considering simultaneously the distribution of the epicenters and the respective focal mechanisms (e.g., Figures 16 and 17), we can say that the NNW–SSE alignment direction of the epicenters is related to the dominant strikes-slip fault solutions on the right and left sides, respectively, while in the center of the Aldeia da Serra zone, in the approximately NNE–SSW direction, the inverse horizontal component dominates. These distinctions of mechanisms in differentiated types suggest that earthquakes are occurring in two distinct faults. Reverse-type dominance mechanisms may be the result of the accommodation of relative movements between the right and left lateral strike-slip structures.
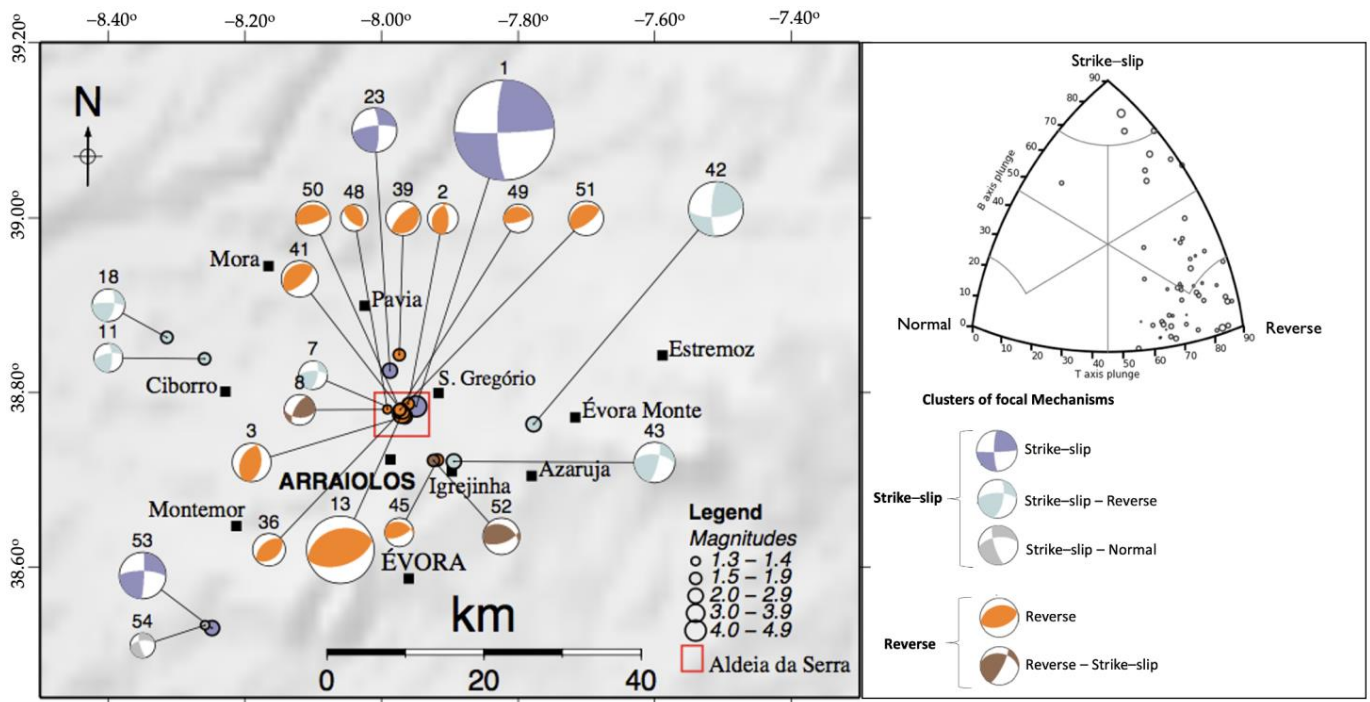

Figure 16. Focal mechanisms of seismic sequence of Arraiolos (period of 15 January–30 June 2018) determined in this study by P-wave polarities and S/P amplitude ratios and triangle diagram to classify focal mechanism [76]. Different colors identify different types of mechanisms: blue = strike-slip faulting (SS); light blue = strike-slip faulting with a minor thrust component (ST); gray = strike-slip faulting with normal component (SN); orange = thrust faulting (TF); brown = thrust faulting with a minor strike-slip component (TS). Only focal mechanisms of events (M ≥ 1.3) are shown in this figure. This event occurred in the Arraiolos region or Arraiolos seismic zone (ASZ), which include the Aldeia da Serra zone (ASZ), Azaruza-Igrejinha zone (AIZ), and Ciborro zone (CZ), respectively. Solution parameters for focal mechanisms are listed in Table A1 (in Appendix A).

The depth distribution of the focal mechanisms of the main shock and the aftershocks in the Aldeia da Serra zone, including the mechanisms of some events in the surroundings of this zone, are illustrated in Figure 17. The focal depths of the Aldeia da Serra Zone are mainly concentrated around 12 km. The distribution of the focal depth seems to reflect well the main features of the lithospheric structure. The earthquakes in this zone are mainly grouped at shallow depths (between 12 and 13 km), while the earthquakes that occur in the remaining zones reach relatively greater depths, probably acting as transition zones between different domains (Section 2).
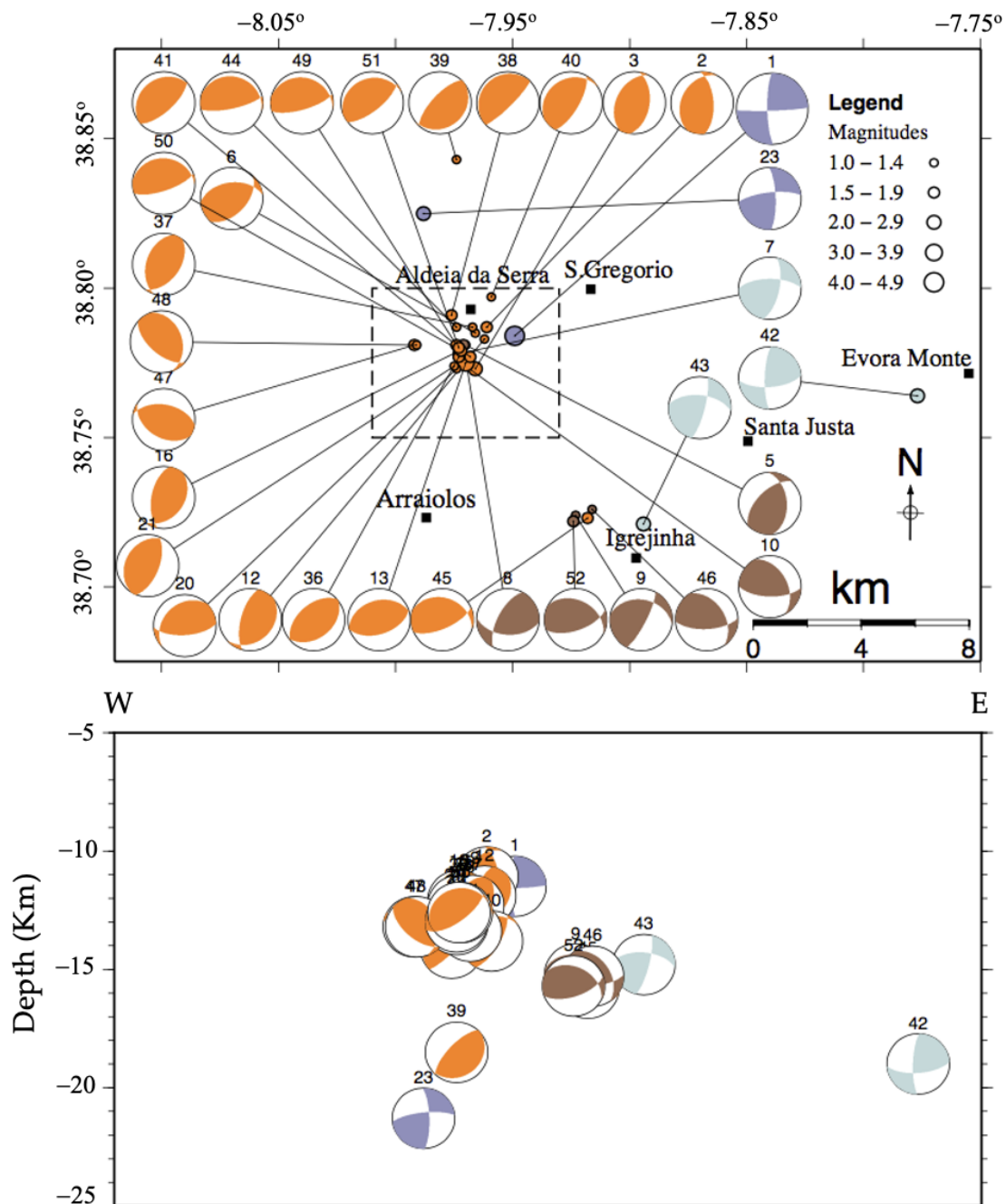
Figure 17. Map showing focal mechanism of main–shock and aftershocks in a more restricted zone of Aldeia da Serra (rectangle), including the Azaruja-Igrejinha zone, and distribution depth of focal mechanisms in of these events (4.9 ≥ M ≥ 1) (cross-section oriented in direction W–E). Different colors identify different types of mechanisms: blue = strike-slip faulting (SS); light blue = strike-slip faulting with a minor thrust component (ST); gray = strike-slip faulting with normal component (SN); orange = thrust faulting (TF); brown = thrust faulting with a minor strike-slip component (TS). The focal mechanisms of aftershocks in Aldeia da Serra with focal depths of 12–13 km, and 14–16 km in Azaruja-Igrejinha zone. Solution parameters for focal mechanisms are listed in Table A1 (in Appendix A).

6. Seismotectonic Implications

The results obtained in this study allowed us to draw a more detailed sketch of the broader geodynamic behavior of the Arraiolos Seismic Zone (which includes the zone of the Aldeia da Serra), illustrated in Figures 18 and 19. In the Aldeia da Serra Seismic Sub-zone,

the earthquakes' focal mechanisms (Figure 18), determined in this study, are characterized by faulting regimes which correspond to strike-slip with a right lateral motion and reverse fault near the Aldeia da Serra escarpment.
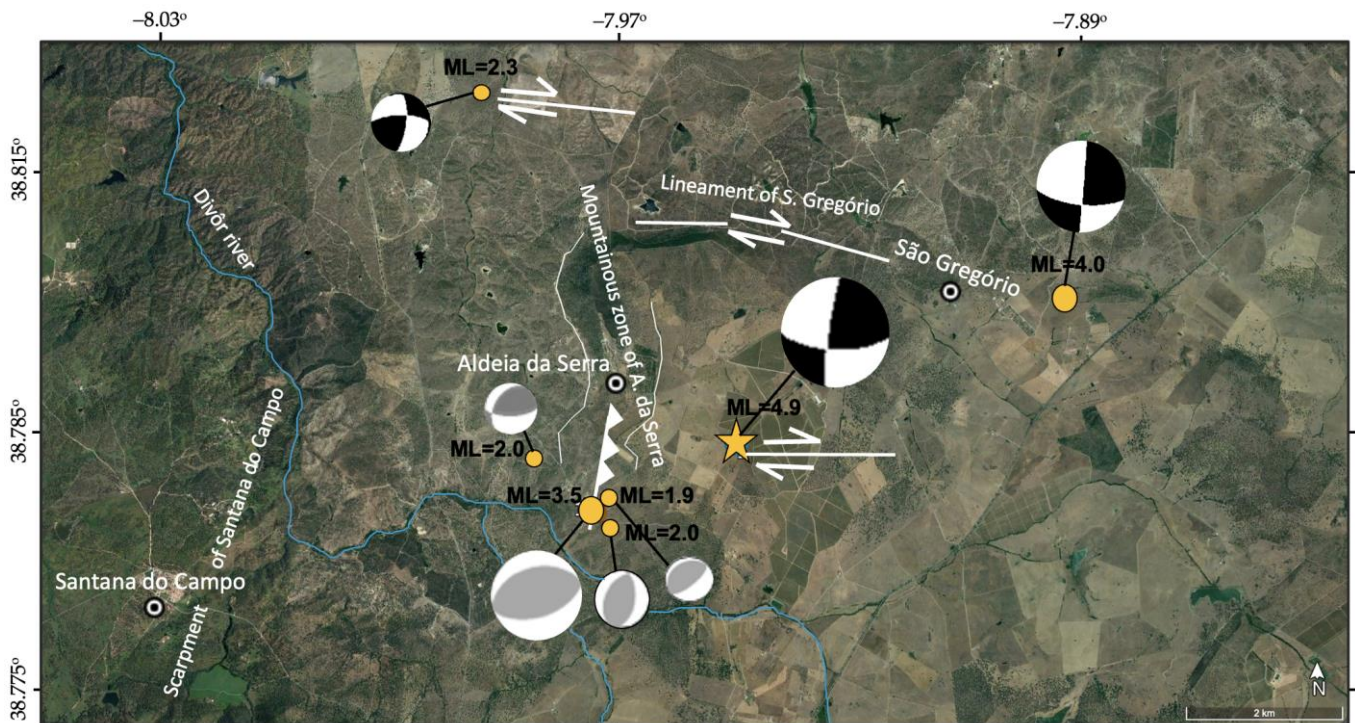

Figure 18. Satellite image of the Aldeia da Serra Seismic Sub-zone—identifies where the main lineaments are represented (in white) and located epicenters (yellow circles) with magnitudes (ML ≥ 1.9) which correspond to strike-slip with right lateral motion and reverse fault near Aldeia da Serra scarp. Yellow star—main earthquake (ML = 4.9). The focal solutions of these earthquakes were determined in this study, with the exception of the magnitude event (ML = 4.0), determined by [1].

In addition to the fault plan solutions determined in this article, we selected from the literature 11 focal mechanisms of superficial earthquakes with magnitudes greater than or equal to 1.5 that occurred in the region of Central Alentejo, which includes the Arraiolos Seismic Zone, during the period of 1987–2012. They are listed and referenced in Table 3. With this set of data, a seismotectonic model of the Seismic Zone of Arraiolos (ASZ) was proposed (Figure 19).

The occurrence of nearby earthquakes with a strike-slip solution and a reverse solution, or a composition of both, seems to agree with the proposal by [8] on the current tectonic activity responsible for the genesis of the Aldeia da Serra escarpment, the upturn to the west, which corresponds to one of the most expressive topographical accidents in that area. This suggests that the two dominant directions of the epicenters (N–S and NNW–SSE, respectively) may have been generated by different structures and probably correspond to a set of different faults reactivated by the main earthquake. One of these directions corresponds to the trend of the NNW–SSE fault system that corresponds to the São Gregório and Ciborro faults, while the second is related to a trend of the N–S fault system that corresponds to the mountainous area of Aldeia da Serra, which possibly constitutes the main seismic source of ASZ, and the seismicity pattern shown in Figures 6–8 (Section 4) also support this indication.
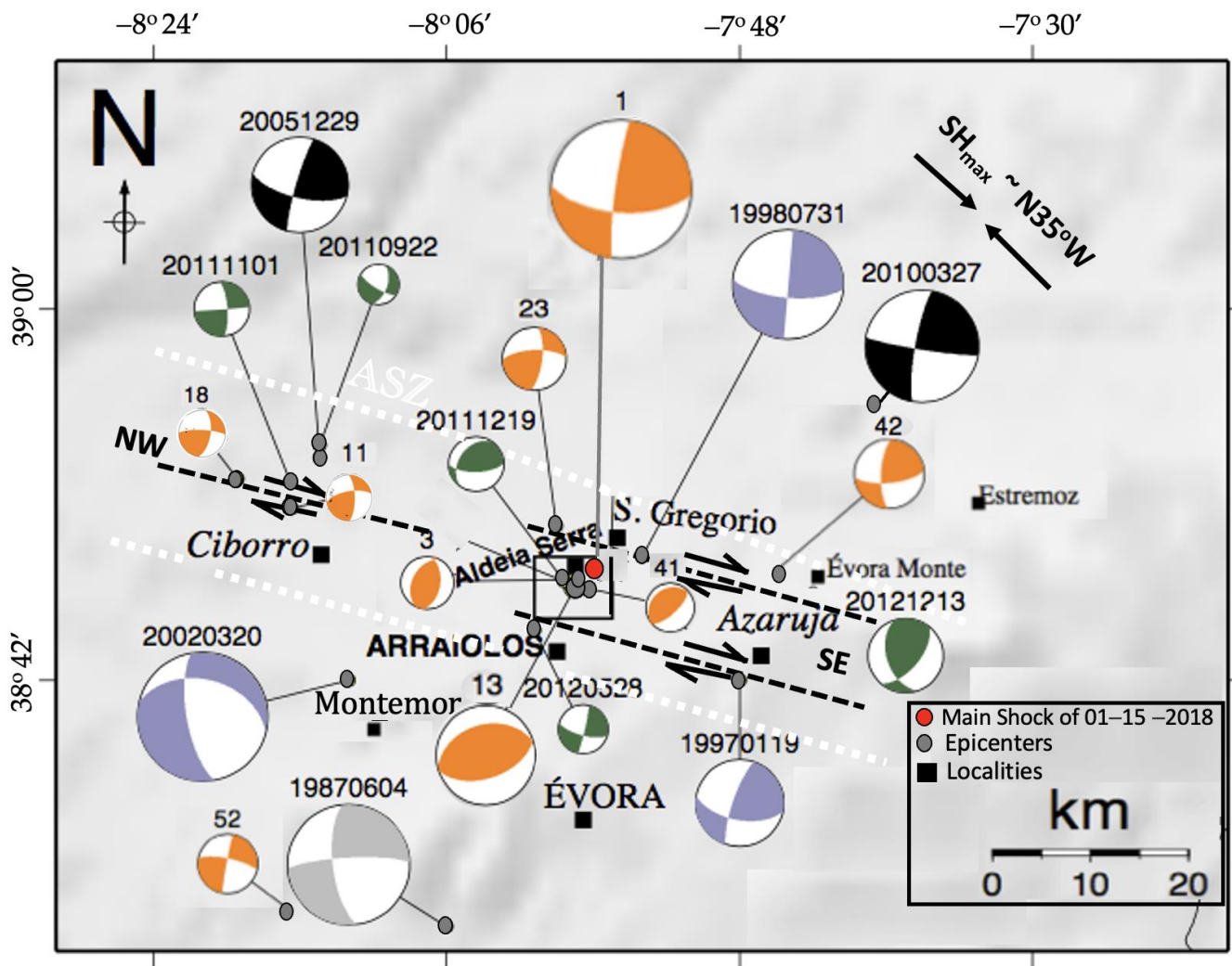
Figure 19. Proposal of the seismotectonic model of the Arraiolos seismic zone (ASZ). These results suggest that this zone constitutes a strike-slip-type shear zone encompassing three segments (black dashed lines), based on the World Stress Map 2016 [75]. The distributions of the focal mechanisms of regional seismic data around the study zone show the predominance of strike-slip mechanisms with possible WNW–ESE and SSW–NNE fault plans. Gray focal mechanisms determined by [38]. Blue determined by [1]. Black published in [77]. Green determined by [10]. Orange focal mechanisms determined in this work.

Table 3. Focal solutions of earthquakes in region, determinate by other authors. MOR [38]; BOR [1]; CUS [77]; MAT [10].

N°	Date (yy/mm/dd)	Hour (hh:mm:ss)	Long. (°W)	Lat. (°N)	Depth (km)	Mag. (ML)	Strike (°)	Dip (°)	Rake (°)	Ref.
1	1987/06/04	-	−8.1	38.5	0	4.4	262	84	−162	MOR
2	1997/01/19	-	−7.8	38.7	13	3.2	100.7	58.8	165.2	BOR
3	1998/07/31	-	−7.9	38.8	5	4.0	95	70	180	BOR
4	2002/03/20	-	−8.2	38.7	12.5	3.7	284	41	−149	BOR
5	2005/12/29	04:25	−8.230	38.880	10.0	3.5	196	83	22	CUS
6	2010/03/27	13:37	−7.613	38.970	14.0	4.1	190	80	5	CUS
7	2012/12/13	13:54:08.54	−7.63	38.72	15.2	2.7	162	48	43	MAT
8	2011/11/01	18:23:41.48	−8.26	38.86	8.8	2.0	86	90	−164	MAT
9	2011/12/19	16:45:20.28	−7.98	38.78	12.8	2.0	89	66	120	MAT
10	2012/05/28	14:37:14.84	−8.01	38.74	19.8	1.8	13	85	−20	MAT
11	2011/09/22	17:42:30.45	−8.23	38.89	23.3	1.5	19	54	−21	MAT

The solutions of the focal mechanisms seem to be dominated by maximum horizontal compressive stresses with a NW–SE tendency, which are compatible with the focal mechanisms determined by other authors in the Arraiolos Seismic Zone (ASZ) and surroundings [1,10,38,77], favorably oriented in relation to the maximum horizontal compressive stress' regional SHmax~N30°W [75]. These directions correspond to the trend of the NNW fault systems—SSE was identified as the Ciborro fault on the left flank of the Aldeia da Serra zone, and on the right flank, corresponds to the lineament of São Gregório, while in the center of Aldeia da Serra, it is related to a trend of the NS fault system, which corresponds to the mountainous area of Aldeia da Serra (the highest point of the region). This geometry can be explained in this tectonic context by the existence of an intersection of faults (probably the escarpment of Aldeia da Serra, or oriented in the N–S direction), with other structures oriented to NNW–SSE or WNW–ESE (Figure 18).

This type of intersection constitutes a structural discontinuity in the propagation of the main fault movement, controlling nucleation and blocking seismic events. Accumulated stresses are usually resolved as small movements, but may have some mild events when the point stress builds up in response to the blockage formed by the second structure to the main movement along the scarp of Aldeia da Serra.

7. Conclusions

The dominance of the reverse fault mechanism in earthquake agglomerates near the mountainous area of Aldeia da Serra suggests a local compression, which favors the topographical elevation of that area. This zone is situated at the confluence of two regional tectonic domains, where the N–S structures shift from the east (north) direction to WNW–ESSE (Lineament of S. Gregório). In this context, the interaction between structures with different orientations can affect the fault kinematics, favoring the appearance of roughness in the active structures of the approximately NNE–SSW trend area (Scarp of Aldeia da Serra). These structurally fragile zones favor, at the same time, the concentration of tensions and control the development of low magnitude seismicity. This means that the seismic activity in this zone, together with the compressive faults in a generally strike-slip environment, suggests a local passage that causes different stresses.

The observed b value of approximately 1.0 suggests a tectonic control for these earthquakes. The seismicity data obtained clearly show the boundary marked by ASZ as a narrow WNW–ESSE oriented seismic belt, and it is a region of slow but active deformation.

The distribution of the focal mechanisms of some regional events (ML $\geq$ 1.5) around the study zone show the predominance of the strike-slip type mechanisms. These data suggest that the Arraiolos Seismic Zone is a shear zone of the right lateral-slip (strike-slip) type, denoting an approximately homogeneous stress pattern, with horizontal compression in the NW $\pm$ SE direction. This is in agreement with the results obtained by [3] for the entire Ibero-Maghreb region and with the orientation of the main tension axis along the boundary of the Eurasian $\pm$ African plate.

In short, this temporary network allowed the detection of several low-magnitude events not detected by the permanent network, significantly lowering the magnitude detection threshold in that zone. The good azimuthal coverage also allowed for good precision in the determination of the hypocenter parameters. The main shock and the respective seismic sequence occurred in a zone of microseismic activity, which had already been identified in several previous studies. Therefore, the seismic tomography studies currently underway in this zone by [13] may provide further interpretations and accurately discover the tectonic processes that generated the seismicity of Arraiolos.

In this study, namely through the patterns delineated from the distribution of the epicenters of the studied sequence and the focal mechanisms, it was possible to clarify the local tectonics and better understand the complexity of the regional tectonics.

Appendix A

Table A1. Parameters of the focal mechanisms of the earthquakes calculated through the polarities of the first arrival movement of the P wave and SH/P amplitude ratios, in the period of 15 January–30 June 2018.

N°	Date (yy/mm/dd)	Hour (hh:mm:ss)	Long. (°W)	Lat. (°N)	Depth (km)	Mag. (ML)	Strike (∅°)	Dip (δ°)	Rake (λ°)	FPU (°) Plane A	Plane B	N pobs/pok	N SH/P	F (σ)	STDR	Er. SH/P	Qs
1	2018/01/15	11:51:40.0	−7.949	38.783	11.8	4.9	88.0	85.8	168.5	2.0	2.7	16/15	3	0.07	0.70	0.34	A
2	2018/01/15	19:47:52.3	−7.961	38.787	11.1	1.6	208.7	34.4	118.0	3.7	15.8	9/9	4	0.00	0.71	0.87	A
3	2018/01/16	02:04:59.2	−7.966	38.773	12.0	2.0	207.0	42.0	104.0	0.0	7.5	10/9	7	0.06	0.68	0.90	A
4	2018/01/17	19:48:40.3	−7.969	38.786	12.4	0.9	202.1	62.0	120.0	1.0	16.7	10/10	10	0.00	0.66	0.77	A
5	2018/01/17	22:32:56.2	−7.970	38.781	12.1	1.0	225.3	57.0	122.7	2.1	18.5	9/9	9	0.00	0.63	0.87	A
6	2018/01/18	06:55:30.9	−7.966	38.785	12.8	1.2	263.2	47.3	120.0	1.2	16.8	12/11	12	0.12	0.68	0.69	A
7	2018/01/23	01:56:47.7	−7.973	38.778	12.3	1.5	269.9	65.5	152.9	1.7	4.8	20/19	19	0.07	0.69	0.74	A
8	2018/01/24	12:58:51.0	−7.971	38.781	12.3	1.6	93.9	50.0	145.0	1.0	12.7	11/11	10	0.00	0.59	0.79	A
9	2018/01/26	03:27:27.7	−7.923	38.724	15.2	1.1	280.2	36.0	159.0	0.0	4.6	13/12	13	0.05	0.78	0.53	A
10	2018/01/26	08:58:32.9	−7.970	38.774	12.2	1.0	331.9	44.0	142.0	0.0	12.1	9/8	9	0.13	0.69	0.84	A
11	2018/01/30	06:33:53.2	−8.259	38.839	9.8	1.5	259.6	66.1	157.3	18.9	32.6	17/17	17	0.00	0.48	0.84	B
12	2018/01/30	15:46:46.1	−7.962	38.783	11.9	1.2	48.9	29.1	120.5	1.1	16.0	14/14	14	0.00	0.72	0.61	A
13	2018/02/01	04:15:42.1	−7.970	38.775	12.4	3.5	255.4	38.0	93.0	0.0	1.0	30/29	29	0.03	0.70	0.64	A
14	2018/02/02	22:45:20.6	−7.973	38.775	12.3	1.0	122.1	77.7	113.8	7.1	13.4	17/17	16	0.00	0.68	0.61	A
15	2018/02/03	04:43:8.2	−7.971	38.780	12.6	1.0	277.3	26.8	104.0	1.9	6.9	17/17	16	0.00	0.65	0.75	A
16	2018/02/04	16:47:49.8	−7.973	38.779	12.1	1.3	37.1	35.1	111.6	2.2	12.1	14/14	12	0.00	0.69	0.76	A
17	2018/02/07	10:40:31.6	−7.969	38.785	12.3	1.0	38.2	54.0	92.0	0.0	0.0	14/13	14	0.09	0.71	0.78	A
18	2018/02/07	17:03:49.2	−8.314	38.863	24.6	1.7	272.2	77.7	149.6	4.4	32.2	18/17	18	0.05	0.63	0.52	A
19	2018/02/07	17:42:23.7	−7.963	38.783	11.8	0.6	52.1	32.0	129.0	0.0	21.9	11/11	10	0.00	0.71	0.68	A
20	2018/02/09	03:10:24.2	−7.974	38.773	12.7	1.1	86.4	65.3	109.4	1.3	10.6	19/18	19	0.06	0.68	0.68	A
21	2018/02/09	03:10:38.1	−7.975	38.774	12.7	1.2	210.0	30.0	97.0	0.0	3.4	14/13	14	0.09	0.70	0.70	A
22	2018/02/09	09:26:38.7	−7.971	38.780	12.3	0.5	99.2	61.0	110.3	1.7	11.1	9/9	9	0.00	0.55	0.80	A
23	2018/02/12	03:35:39.3	−7.988	38.825	21.3	2.3	263.9	74.0	164.6	1.0	2.2	26/25	13	0.03	0.71	0.30	A
24	2018/02/14	04:29:52.1	−7.972	38.780	12.5	0.5	277.8	23.9	115.2	2.0	14.2	12/12	12	0.00	0.69	0.70	A
25	2018/02/14	12:47:37.5	−7.971	38.779	12.5	0.6	47.5	53.0	109.5	1.1	10.7	11/10	10	0.13	0.71	0.73	A
26	2018/02/15	02:00:2.8	−7.970	38.779	12.6	0.5	95.9	58.0	111.0	1.0	11.6	12/11	6	0.11	0.68	0.74	A
27	2018/02/17	04:17:28.1	−7.971	38.780	12.4	0.1	274.8	28.0	110.0	7.8	19.0	11/11	5	0.00	0.77	0.53	A
28	2018/02/17	04:25:2.1	−7.970	38.779	12.1	0.4	93.0	42.0	132.0	0.0	5.2	16/15	7	0.09	0.71	0.67	A
29	2018/02/19	05:51:46.5	−7.972	38.779	12.5	0.6	87.9	70.0	110.0	1.6	11.0	18/17	18	0.07	0.72	0.65	A
30	2018/02/19	0618 53.7	−7.971	38.780	12.4	0.1	249.0	20.1	107.2	2.0	5.3	14/12	14	0.16	0.70	0.62	A
31	2018/02/19	06:19:24.7	−7.973	38.779	12.4	0.1	245.6	17.7	102.0	3.8	12.3	12/11	12	0.08	0.69	0.55	A
32	2018/02/19	13:17:30.2	−7.965	38.782	12.0	0.2	44.5	32.0	127.0	0.0	20.8	12/12	11	0.00	0.73	0.59	A
33	2018/02/19	15:51:24.2	−7.971	38.778	12.3	0.2	88.2	67.2	126.8	7.6	11.8	11/10	11	0.11	0.75	0.52	A
34	2018/02/21	20:20:40.4	−7.971	38.780	12.3	0.2	248.0	17.4	101.7	1.2	6.5	12/11	12	0.08	0.72	0.59	A
35	2018/02/23	16:39:42.1	−7.971	38.779	12.2	0.1	316.9	14.6	131.1	1.4	18.9	10/10	10	0.00	0.78	0.54	A
36	2018/02/24	10:52:9.6	−7.973	38.777	12.3	1.7	52.8	40.0	93.0	0.0	1.0	15/14	14	0.03	0.70	0.56	A
37	2018/02/25	00:27:45.6	−7.967	38.787	12.3	1.0	36.3	48.0	102.0	0.0	4.0	13/12	10	0.02	0.65	0.82	A
38	2018/03/29	13:29:14.1	−7.976	38.791	14.1	1.8	229.4	10.0	94.0	0.0	1.6	9/8	8	0.05	0.66	0.63	A
39	2018/03/29	21:46:1.5	−7.974	38.843	18.5	1.4	52.9	20.9	99.3	11.7	7.9	8/7	7	0.13	0.82	0.23	A
40	2018/04/14	21:38:51.2	−7.959	38.797	13.8	1.0	239.4	23.0	117.3	1.8	15.2	8/8	6	0.00	0.60	0.98	A

Table A1. *Cont.*

N°	Date (yy/mm/dd)	Hour (hh:mm:ss)	Long. (°W)	Lat. (°N)	Depth (km)	Mag. (ML)	Strike (∅°)	Dip (δ°)	Rake (λ°)	FPU (°) Plane A	Plane B	N pobs/pok	N SH/P	F (σ)	STDR	Er. SH/P	Qs
41	2018/04/28	03:39:21.9	−7.968	38.777	13.4	1.9	234.6	22.4	96.2	1.4	4.4	11/10	8	0.08	0.65	0.63	A
42	2018/05/09	23:27:12.2	−7.777	38.764	19.0	2.8	85.6	66.0	165.0	0.0	15.0	14/14	8	0.07	0.52	0.59	A
43	2018/05/10	14:36:13.1	−7.894	38.721	14.8	2.1	275.9	57.1	164.6	1.0	2.1	12/11	6	0.06	0.61	0.64	A
44	2018/05/26	21:04:29.7	−7.974	38.787	13.1	1.2	287.2	16.9	118.3	1.6	16.2	9/9	7	0.00	0.72	0.61	A
45	2018/05/29	19:48:56.6	−7.918	38.723	15.8	1.5	289.1	30.6	128.5	1.1	7.2	9/8	5	0.08	0.59	1.08	A
46	2018/05/29	21:38:29.7	−7.916	38.726	15.3	1.1	326.9	42.5	141.9	3.1	10.5	8/7	7	0.15	0.56	0.58	A
47	2018/05/31	02:41:37.2	−7.992	38.781	13.2	1.6	121.5	42.0	106.5	1.0	9.0	11/10	7	0.03	0.66	0.54	A
48	2018/06/01	02:40:32.9	−7.991	38.781	13.2	1.4	341.3	34.5	115.8	12.8	17.9	8/8	7	0.00	0.71	0.59	A
49	2018/06/01	21:04:33.7	−7.974	38.781	13.0	1.5	281.6	20.0	116.0	0.0	14.4	9/8	8	0.15	0.68	0.73	A
50	2018/06/03	21:00:18.7	−7.972	38.779	12.6	1.8	275.8	20.0	113.0	0.0	12.7	9/9	8	0.00	0.69	0.78	A
51	2018/06/03	21:00:50.9	−7.973	38.780	12.6	1.8	251.2	22.0	108.0	0.0	9.8	9/9	8	0.00	0.70	0.77	A
52	2018/06/11	21:47:11.2	−7.924	38.722	15.7	1.9	297.6	38.0	130.0	0.0	1.6	10/9	5	0.14	0.62	0.88	A
53	2018/06/27	03:24:22.5	−8.248	38.530	14.4	2.4	271.1	72.5	174.4	6.1	17.3	17/16	8	0.04	0.57	0.86	A
54	2018/06/27	05:17:28.1	−8.258	38.533	15.0	1.3	263.0	57.0	−161.6	6.8	34.6	10/10	4	0.00	0.63	0.79	B

Note: FPU—Estimate of the uncertainties of fault-plane solution (Plane A and B). N_{pobs} is the number of observed polarities and N_{pok} is the number of correct polarities. $N_{SH/P}$—Number of measuring amplitude ratios. F(σ)—Weighted fraction of polarity deviations (misfit). STDR—Stations distribution ratio; Er. SH/P—Average amplitude error. Q_s—Quality of the solution of focal mechanism based on the criteria proposed by Hardebeck and Shearer [20].

References

1. Borges, J.F.; Fitas, A.J.; Bezzeghoud, M.; Teves-Costa, P. Seismotectonics of Portugal and its adjacent Atlantic area. *Tectonophysics* **2001**, *331*, 373–387. [CrossRef]
2. Bezzeghoud, M.; Borges, J.F.; Caldeira, B. Fontes sísmicas ao longo da fronteira de placas tectónicas entre os Açores e a Argélia: Um modelo sismotectónico. In *Geologia de Portugal, Volume II—Geologia Meso-Cenozóica de Portugal*; Escolar Editora: Forte da Casa, Portugal, 2013.
3. Bezzeghoud, M.; Buforn, E. Source parameters of the 1992 Melilla (Spain, *MW* = 4.8), 1994 Alhoceima (Morocco, *MW* = 5.8), and 1994 Mascara (Algeria, *MW* = 5.7) earthquakes and seismotectonic implications. *Bull. Seismol. Soc. Am.* **1999**, *89*, 359–372. [CrossRef]
4. Kilb, D.; Gomberg, J.; Bodin, P. Triggering of earthquake aftershocks by dynamic stresses. *Nature* **2000**, *408*, 570–574. [CrossRef] [PubMed]
5. Buforn, E.; Udías, A. Sismicidad y mecanismo focal de los terremotos de la región Cabo de San Vicente-Argelia. *Rev. Soc. Geológica España* **2007**, *20*, 301–310.
6. Toda, S.; Enescu, B. Rate/state Coulomb stress transfer model for the CSEP Japan seismicity forecast. *Earth Planets Space* **2011**, *63*, 171–185. [CrossRef]
7. Lentas, K. Towards routine determination of focal mechanisms obtained from first motion P-wave arrivals. *Geophys. J. Int.* **2018**, *212*, 1665–1686. [CrossRef]
8. Araújo, A.; Matos, C.; Martins, A. A elevação de Aldeia da Serra (Arraiolo s): Um "push up" activo associado à Falha de Ciborro e ao lineamento de S. Gregório? e-Terra: Revista Electrónica de Ciências da Terra. In *VIII Congresso Nacional de Geologia*; E-Terra: Braga, Portugal, 2010; Volume 11, ISSN 1645-0388.
9. Wachilala, P.E. Sismotectónica da Região de Ciborro-Arraiolos e Sua Relação com a Geomorfologia Local. Master's Thesis, Universidade de Évora, Évora, Portugal, 2015. (In Portuguese)
10. Matos, C.; Custódio, S.; Batlló, J.; Zahradník, J.; Arroucau, P.; Silveira, G.; Heimann, S. An active seismic zone in intraplate west Iberia inferred from high resolution geophysical data. *J. Geophys. Res.* **2018**, *123*, 2885–2907. [CrossRef]
11. Matias, L.; Rio, I.; Wachilala, P.; Vales, D.; Borges, J.; Dias, N.; Carrilho, F.; Caldeira, B.; Custodio, S.; Fontiela, J.; et al. The seismic sequence of Arraiolos, Portugal, in January 2018. In Proceedings of the 21st EGU General Assembly, EGU2019, Vienna, Austria, 7–12 April 2019; Volume 21.
12. Wachilala, P.; Borges, J.F.; Caldeira, B.; Matias, L.; Rio, I.; Bezzeghoud, M. Seismotectonic characterization of the region of Arraiolos, South Portugal: Period of January–May, 2018. In Proceedings of the 27th IUGG General Assembly, Montréal, QC, Canada, 8–18 July 2019; p. S01p-371.
13. Hamak, I.; Wachilala, P.; Borges, J.; Dias, N.; Rio, I.; Bezzeghoud, M. Improved three-dimensional image of the tomographic inversion of the Arraiolos aftershock sequence. In Proceedings of the EGU General Assembly 2021, Online, 19–30 April 2021; p. EGU21-8079.
14. Barfal, S.S.; Das, M.M.; Joshi, M.; Joshi, R.; Kumar, K.; Kumar, D.; Rai, Y.K. Response of water springs towards an earthquake: A case study from Sikkim Himalaya. *J. Appl. Geophys.* **2022**, *206*, 104792. [CrossRef]
15. Tajima, F.; Kanamori, H. Global survey of aftershock area expansion patterns. *Phys. Earth Planet. Inter.* **1985**, *40*, 77–134. [CrossRef]
16. Kilb, D.; Rubin, A.M. Implications of diverse fault orientations imaged in relocated aftershocks of the Mount Lewis, M_L5.7, California, earthquake. *J. Geophys. Res. Atmos.* **2002**, *107*, 2294. [CrossRef]
17. Yang, H.; Zhu, L.; Chu, R. Fault-Plane Determination of the 18 April 2008 Mount Carmel, Illinois, Earthquake by Detecting and Relocating Aftershocks. *Bull. Seismol. Soc. Am.* **2009**, *99*, 3413–3420. [CrossRef]
18. Freed, A.M. Earthquake triggering by static, dynamic, and postseismic stress transfer. *Annu. Rev. Earth Planet. Sci.* **2005**, *33*, 335–367. [CrossRef]
19. Tang, C.-C.; Lin, C.-H.; Peng, Z. Spatial-temporal evolution of early aftershocks following the 2010 ML 6.4 Jiashian earthquake in southern Taiwan. *Geophys. J. Int.* **2014**, *199*, 1772–1783. [CrossRef]
20. Lin, G.; Okubo, P.G. A large refined catalog of earthquake relocations and focal mechanisms for the Island of Hawai'i and its seismotectonic implications. *J. Geophys. Res. Solid Earth* **2016**, *121*, 5031–5048. [CrossRef]
21. Hardebeck, J.L.; Shearer, P.M. A new method for determining first-motion focal mechanisms. *Bull. Seismol. Soc. Am.* **2002**, *92*, 2264–2276. [CrossRef]
22. Kilb, D.; Hardebeck, J.L. Fault Parameter Constraints Using Relocated Earthquakes: Validation of First Motion Focal Mechanism Data. *Bull. Seismol. Soc. Am.* **2006**, *96*, 1140–1158. [CrossRef]
23. Hardebeck, J.L.; Shearer, P.M. Using S/P Amplitude Ratios to Constrain the Focal Mechanisms of Small Earthquakes. *Bull. Seismol. Soc. Am.* **2003**, *93*, 2434–2444. [CrossRef]
24. Ribeiro, A.; Quesada, C.; Dallmeyer, R.D. Geodynamic evolution of the Iberian Massif. In *Pre-Mesozoic Geology of Iberia*; Dallmeyer, R.D., Martínez-García, E., Eds.; Springer: Berlin/Heidelberg, Germany, 1990; pp. 397–410.
25. Matte, P. The Variscan collage and orogeny (480–290 Ma) and the tectonic definition of the Armorica microplate: A review. *Terra Nova* **2001**, *13*, 122–128. [CrossRef]
26. Pous, J.; Poyatos, D.M.; Heise, W.; Santos, F.M.; Galindo-Zaldívar, J.; Ibarra, P.; Pedrera, A.; Ruiz-Constán, A.; Anahnah, F.; Gonçalves, R.; et al. Constraints on the crustal structure of the internal Variscan Belt in SW Europe: A magnetotelluric transect along the eastern part of Central Iberian Zone, Iberian Massif. *J. Geophys. Res. Atmos.* **2011**, *116*, B02103. [CrossRef]

27. Pérez-Estaún, A.; Bea, F.; Bastida, F.; Marcos, A.; Martínez, C.J.R.; Martínez, P.D.; Arenas, R.; Díaz, G.F.; Azor, A.; Simancas, J.F.; et al. La cordllera varisca europea: El Macizo Ibérico. In *Geología de España. Society Geology*; Vera, J.A., Ed.; IGME: Madrid, Spain, 2004; pp. 21–25.

28. Pereira, M.F.; Chichorro, M.; Moita, P.; Santos, J.F.; Solá, A.M.R.; Williams, I.S.; Silva, J.B.; Armstrong, R.A. The multistage crystallization of zircon in calc-alkaline granitoids: U–Pb age constraints on the timing of Variscan tectonic activity in SW Iberia. *Int. J. Earth Sci.* **2015**, *104*, 1167–1183. [CrossRef]

29. Simancas, J.F.; Carbonell, R.; González Lodeiro, F.; Pérez Estaún, A.; Juhlin, C.; Ayarza, P.; Kashubin, A.; Azor, A.; Martínez Poyatos, D.; Almodovar, G.R.; et al. Crustal structure of the transpressional Variscan orogen of SW Iberia: SW Iberia deep seismic reflection profile (IBERSEIS). *Tectonics* **2003**, *22*, 1062. [CrossRef]

30. Carbonell, R.; Simancas, F.; Juhlin, C.; Pous, J.; Pérez-Estaún, A.; Gonzalez-Lodeiro, F.; Muñoz, G.; Heise, W.; Ayarza, P. Geophysical evidence of a mantle derived intrusion in SW Iberia. *Geophys. Res. Lett.* **2004**, *31*, L11601. [CrossRef]

31. Palomeras, I.; Carbonell, R.; Ayarza, P.; Fernàndez, M.; Simancas, J.; Poyatos, D.M.; Lodeiro, F.G.; Pérez-Estaún, A. Geophysical model of the lithosphere across the Variscan Belt of SW-Iberia: Multidisciplinary assessment. *Tectonophysics* **2011**, *508*, 42–51. [CrossRef]

32. Brown, D.; Zhang, X.; Palomeras, I.; Simancas, F.; Carbonell, R.; Juhlin, C.; Salisbury, M. Petrophysical analysis of a mid-crustal reflector in the IBERSEIS profile, SW Spain. *Tectonophysics* **2012**, *550–553*, 35–46. [CrossRef]

33. Argus, D.F.; Gordon, R.G.; DeMets, C.; Stein, S. Closure of the Africa-Eurasia-North America Plate motion circuit and tectonics of the Gloria Fault. *J. Geophys. Res. Atmos.* **1989**, *94*, 5585–5602. [CrossRef]

34. DeMets, C.; Gordon, R.G.; Argus, D.F.; Stein, S. Effect of recent revisions to the geo- magnetic reversal time scale on estimates of current plate motions. *Geophys. Res. Lett.* **1994**, *21*, 2191–2194. [CrossRef]

35. DeMets, C.; Gordon, R.G.; Argus, D.F. Geologically current plate motions. *Geophys. J. Int.* **2010**, *181*, 1–80. [CrossRef]

36. Nocquet, J.-M. Present-day kinematics of the Mediterranean: A comprehensive overview of GPS results. *Tectonophysics* **2012**, *579*, 220–242. [CrossRef]

37. Attanayake, J.; Ferreira, A.M.; Berbellini, A.; Morelli, A. Crustal structure beneath Portugal from teleseismic Rayleigh Wave Ellipticity. *Tectonophysics* **2017**, *712–713*, 344–361. [CrossRef]

38. Moreira, V.S. Historical seismicity and seismotectonics of the area situated between the Iberian Peninsula, Marrocco, Selvagens and Azores Islands. In *Seismicity, Seismotectonic and Seismic Risk of the Ibero-Magrebian Region*; IGN: Urbana, IL, USA, 1991; Volume 8, pp. 213–225.

39. Zbyszewski, G.; Barros, A.; Da Veiga Ferreira, O. *Carta Geológica de Portugal na Escala 1/50 000, folha 36-A (Pavia) e Respectiva Notícia Explicativa*; Direcção Geral de Geologia e Minas, Serviços Geológicos de Portugal: Lisboa, Portugal, 1980.

40. Moita, P. Granitóides no SW da Zona de Ossa-Morena (Montemor o Novo–Évora): Petrogénese e Processos Geodinâmicos. Ph.D. Thesis, Universidade de Évora, Évora, Portugal, 2007; p. 351.

41. Oliveira, J.T.; Pereira, E.; Ramalho, M.; Antunes, M.T.; Monteiro, J.H. (Eds.) *Carta Geológica de Portugal à escala 1/500.000*, 5th ed.; Serviços Geológicos de Portugal: Lisboa, Portugal, 1992.

42. Feio, M.; Martins, A. *O Relevo do Alto Alentejo, (Traços Essenciais)*; Finisterra: Lisboa, Portugal, 1993; Volume XXVIII, pp. 149–199.

43. Duarte, I.M.R. Solos Residuais de Rochas Granitóides a Sul do Tejo. Características Geológicas e Geotécnicas. Ph.D. Thesis, Universidade de évora, Évora, Portugal, 2002; 76p. (In Portuguese)

44. Carvalhosa, A.B. *Carta Geológica de Portugal à escala de 1/50,000. Notícia explicativa da folha 36-C, Arraiolos*; Serviços Geológicos de Portugal: Lisboa, Portugal, 1999; 52p.

45. Ottemöller, L.; Voss, P.; Havskov, J. *SEISAN Earthquake Analysis Software for Windows, Solaris, Linux and MacOSX*, Version 10.3; University of Bergen: Bergen, Norway, 2014.

46. Lienert, B.R.; Berg, E.; Frazer, L.N. HYPOCENTER: An earthquake location method using centered, scaled, and adaptively damped least squares. *Bull. Seismol. Soc. Am.* **1986**, *76*, 771–783. [CrossRef]

47. Lienert, B.R.E. *Report on Modifications made to Hypocenter*; Technical report; Institute of Solid Earth Physics, University of Bergen: Bergen, Norway, 1991.

48. Lienert, B.R.; Havskov, J. A Computer Program for Locating Earthquakes Both Locally and Globally. *Seismol. Res. Lett.* **1995**, *66*, 26–36. [CrossRef]

49. Kissling, E. *Program VELEST USER'S GUIDE—Short Introduction*; Technical report; Institute of Geophysics, ETH Zurich: Zurich, Switzerland, 1995.

50. Dias, N.A. Estudo da Sequência Sísmica Gerada Pelo Sismo do Faial de 9 de Julho de 1998: Anisotropia Crustal, Inversão Tomográfica e Caracterização Sismo-Tectónica. Ph.D. Thesis, Universidade de Lisboa, Lisboa, Portugal, 2005. (In Portuguese)

51. Veludo, I.; Dias, N.A.; Fonseca, P.E.; Matias, L.; Carrilho, F.; Haberland, C.; Villaseñor, A. Crustal seismic structure beneath Portugal and southern Galicia (Western Iberia) and the role of Variscan inheritance. *Tectonophysics* **2017**, *717*, 645–664. [CrossRef]

52. Mogi, K. Some discussions on aftershocks, foreshocks and earthquake swarms: The fracture of a semi-infinite body caused by an inner stress origin and its relation to the earthquake phenomena (third paper). *Bull. Earthquake Res. Inst.* **1963**, *41*, 615–658.

53. Utsu, T.; Ogata, Y.; Matsu'ura, R.S. The centenary of the Omori formula for a decay law of after- shock activity. *J. Phys. Earth.* **1995**, *43*, 1–33. [CrossRef]

54. Gutenberg, B.; Richter, C.F. Frequency of earthquakes in California. *Bull. Seismol. Soc. Am.* **1944**, *34*, 185–188. [CrossRef]

55. Mogi, K. Magnitude-Frequency Relation for Elastic Shocks Accompanying Fractures of Various Materials and some Related Problems in Earthquakes. *Bull. Earthq. Res. Inst.* **1962**, *40*, 831–853.
56. Scholz, C.H. The Frequency-Magnitude Relation of Microfracturing in Rock and its Relation to Earth- quakes. *Bull. Seismol. Soc. Am.* **1968**, *58*, 399–415. [CrossRef]
57. Warren, N.W.; Latham, G.V. An experimental study of thermally induced microfracturing and its relation to volcanic seismicity. *J. Geophys. Res. Atmos.* **1970**, *75*, 4455–4464. [CrossRef]
58. El-Isa, Z.H.; Eaton, D.W. Spatiotemporal variations in the b-value of earthquake magnitude–frequency distributions: Classification and causes. *Tectonophysics* **2014**, *615*, 1–11. [CrossRef]
59. Kagan, Y. Universality of the seismic moment-frequency relation. In *Seismicity Patterns, Their Statistical Significance and Physical Meaning*; Pageoph Topical; Springer: Basel, Switzerland, 1999; pp. 537–573.
60. Okal, E.A.; Sweet, J.R. *Frequency-Size Distributions for Intraplate Earthquakes*; Geological Society of America: Boulder, CO, USA, 2007; Volume 425, pp. 59–71.
61. Bachmann, C.E.; Wiemer, S.; Goertz-Allmann, B.P.; Woessner, J. Influence of pore-pressure on the event-size distribution of induced earthquakes. *Geophys. Res. Lett.* **2012**, *39*, L09302. [CrossRef]
62. Wiemer, S.; McNutt, S.R. Variations in the frequency-magnitude distribution with depth in two volcanic areas: Mount St. Helens, Washington, and Mt. Spurr, Alaska. *Geophys. Res. Lett.* **1997**, *24*, 189–192. [CrossRef]
63. Nakajima, J.; Matsuzawa, T.; Hasegawa, A.; Zhao, D. Three dimensional structures of Vp, Vs, and Vp/Vs beneath the northeastern Japan arc: Implications for arc magmatism and fluids. *J. Geophys. Res.* **2011**, *106*, 21843–21857. [CrossRef]
64. Wiemer, S.; Benoit, J.P. Mapping the B-value anomaly at 100 km depth in the Alaska and New Zealand Subduction Zones. *Geophys. Res. Lett.* **1996**, *23*, 1557–1560. [CrossRef]
65. Wyss, M.; Hasegawa, A.; Nakajima, J. Source and path of magma for volcanoes in the subduction zone of northeastern Japan. *Geophys. Res. Lett.* **2001**, *28*, 1819–1822. [CrossRef]
66. Reasenberg, P.; Oppenheimer, D. *FPFIT, FPPLOT, and FPPAGE: FORTRAN Computer Programs for Calculating and Displaying Earthquake Fault-Plane Solutions*; USGS: Lawrence, KS, USA, 1985; pp. 85–739. [CrossRef]
67. Nakamura, M. Determination of focal mechanism solution using initial motion polarity of P and S waves. *Phys. Earth Planet. Inter.* **2002**, *130*, 17–29. [CrossRef]
68. Lund, B.; Boovarsson, R. Correlation of microearthquake body-wave spectral amplitudes. *Bull. Seismol. Soc. Am.* **2002**, *92*, 2419–2433. [CrossRef]
69. Kisslinger, C. Evaluation of S to P amplitude ratios for determining focal mechanisms from regional network observations. *Bull. Seismol. Soc. Am.* **1980**, *70*, 999–1014. [CrossRef]
70. Julian, B.R.; Foulger, G.R. Earthquake mechanisms from linear-programming inversion of seismic-wave amplitude ratios. *Bull. Seismol. Soc. Am.* **1996**, *86*, 972–980. [CrossRef]
71. Dreger, D.; Helmberger, D. Determination of source parameters at regional distances with three-component sparse network data. *J. Geophys. Res.* **1993**, *98*, 8107–8125. [CrossRef]
72. Fukuyama, E.; Ellsworth, W.; Waldhauser, F.; Kubo, A. Detailed fault structure of the 2000 western Tottori, Japan, earthquake sequence. *Bull. Seismol. Soc. Am.* **2003**, *93*, 1468–1478. [CrossRef]
73. Presti, D.; Billi, A.; Orecchio, B.; Totaro, C.; Faccenna, C.; Neri, G. Earthquake focal mechanisms, seismogenic stress, and seismotectonics of the Calabrian Arc, Italy. *Tectonophysics* **2013**, *602*, 153–175. [CrossRef]
74. Shearer, P.M.; Hardebeck, J.L.; Astiz, L.; Richards-Dinger, K.B. Analysis of similar event clusters in aftershocks of the 1994 Northridge, California, earthquake. *J. Geophys. Res. Atmos.* **2003**, *108*, B1. [CrossRef]
75. Heidbach, O.; Rajabi, M.; Reiter, K.; Ziegler, M. *World Stress Map 2016*; GFZ Data Service: Potsdam, Germany, 2016.
76. Álvarez-Gómez, J.A. FMC: A one-liner Python program to manage, classify and plot focal mechanisms data. *Geophy. Res. Abst.* **2014**, *16*, EGU2014-10887.
77. Custódio, S.; Dias, N.; Carrilho, F.; Góngora, E.; Rio, I.; Marreiros, C.; Morais, I.; Alves, P.; Matias, L. Earthquakes in western Iberia: Improving the understanding of lithospheric deformation in a slowly deforming region. *Geophys. J. Int.* **2015**, *203*, 127–145. [CrossRef]